Hybrid simulation of mode conversion at the magnetopause

Y. Lin,[1] J. R. Johnson,[2] and X. Y. Wang[1]

[1] Two-dimensional hybrid simulations are used to investigate how fast-mode compressional waves incident on a magnetopause current layer mode convert both linearly and nonlinearly to short wavelength ($k_\perp \rho_i \sim 1$) kinetic Alfvén waves near the Alfvén resonance surface. The background magnetic fields on both sides of the current layer are parallel to each other and perpendicular to the magnetopause normal, corresponding to a northward interplanetary magnetic field. The simulations are performed in a 2-D plane (xz), where x is normal to the magnetopause and z is tilted by an angle, θ, relative to the magnetic field. We examine how the mode conversion depends on wave frequency ω_0, wave vector, Alfvén velocity profile (particularly the magnetopause width, D_0), ion β in the magnetosheath, electron-to-ion temperature ratio, and incident wave amplitude. Kinetic effects resolve the resonance, and KAWs radiate back to the magnetosheath side of the current layer. The compressional wave absorption rate is estimated and compared with linear theory. Unlike the prediction from low-frequency theory of the Alfvén resonance, KAWs are also generated in cases with $\theta = 0°$, provided $\omega_0 > 0.1\Omega_0$, with Ω_0 being the ion cyclotron frequency in the magnetosheath. As the incident wave amplitude is increased, several nonlinear wave properties are manifested in the mode conversion process. Harmonics of the driver frequency are generated. As a result of nonlinear wave interaction, the mode conversion region and its spectral width are broadened. The nonlinear waves provide a significant transport of momentum across the magnetopause and are associated with significant ion heating in the resonant region.

1. Introduction

[2] Transport of mass, momentum, and energy at the magnetopause boundary drives much of the magnetospheric dynamics and is therefore an important topic in magnetospheric physics. The coexistence of the solar wind and magnetospheric populations in the magnetopause boundary layer and the thickening of the magnetopause boundary layer during periods of northward interplanetary magnetic field (IMF) indicate the existence of efficient transport processes across the magnetopause [*Fujimoto et al.*, 1998; *Phan et al.*, 2000; *Hasegawa et al.*, 2002a, 2002b; *Wing and Newell*, 2002; *Øieroset et al.*, 2003; *Hasegawa et al.*, 2003; *Wing and Newell*, 2003; *Wang et al.*, 2007; *Johnson and Wing*, 2009]. There is evidence that magnetosheath plasma may enter the plasma sheet as the result of cusp reconnection [*Song and Russell*, 1992; *Raeder et al.*, 1997; *Le et al.*,

1996; *Øieroset et al.*, 2003, 2005; *Lavraud et al.*, 2006] and plasma mixing and/or reconnection in Kelvin-Helmholtz vortices [*Ogilvie and Fitzenreiter*, 1989; *Thomas and Winske*, 1991, 1993; *Fairfield et al.*, 2000; *Otto and Fairfield*, 2000; *Nykyri and Otto*, 2001; *Nakamura and Fujimoto*, 2002; *Fujimoto et al.*, 2003; *Fairfield et al.*, 2003, 2007; *Fujimoto et al.*, 2003; *Hasegawa et al.*, 2004, 2006; *Nykyri et al.*, 2006; *Chaston et al.*, 2007]. Another source for plasma entry results from wave-particle diffusive processes in large-amplitude ultralow frequency waves that are frequently observed at the magnetopause boundary [*Anderson et al.*, 1982; *Tsurutani and Thorne*, 1982; *Rezeau et al.*, 1986; *Labelle and Treumann*, 1988; *Rezeau et al.*, 1989; *Engebretson et al.*, 1991b, 1991a; *Lin et al.*, 1991; *Takahashi et al.*, 1991; *Rezeau et al.*, 1993; *Song et al.*, 1993c, 1993b, 1993a; *Anderson et al.*, 1994; *Song*, 1994; *Song et al.*, 1994; *Phan et al.*, 1994, 1996a, 1996b]. One of the more common spectral features at the magnetopause boundary is the sharp transition in wave polarization from compressional, e.g., because of foreshock waves of the quasi-parallel bow shock, to transverse waves from the magnetosheath to the boundary layers [*Johnson and Cheng*, 1997; *Johnson et al.*, 2001; *Chaston et al.*, 2008, and references therein]. It has been suggested that the mode

[1] Physics Department, Auburn University, Auburn, Alabama, USA.
[2] Princeton Plasma Physics Laboratory, Princeton University, Princeton, New Jersey, USA.

conversion from compressional to Alfven modes provides a source of Alfvén waves at the magnetopause, which can efficiently transport plasma across the magnetopause boundary [*Hasegawa and Mima*, 1978; *Lee et al.*, 1994; *Johnson and Cheng*, 1997; *Chen*, 1999; *Johnson et al.*, 2001; *Chaston et al.*, 2008]. Multipoint measurements have verified that the dispersion of the broadband waves is consistent with the kinetic Alfvén waves [*Chaston et al.*, 2007, 2008]. Such mode conversion may lead to effective heating and transport of plasma at the magnetopause [*Hasegawa and Mima*, 1978; *Johnson and Cheng*, 1997; *Chen*, 1999; *Johnson and Cheng*, 2001; *Chaston et al.*, 2008]. Kinetic Alfvén waves also provide a natural explanation for the observed dawn-dusk asymmetry in plasma entry during northward IMF [*Hasegawa et al.*, 2003; *Wing et al.*, 2005] because they result from mode conversion of compressional foreshock waves, which typically bathe the dawn flank for the typical Parker spiral configuration.

[3] According to linear theory, when an magnetohydrodynamic (MHD) fast mode compressional wave propagates across in an inhomogeneous plasma, it is coupled with the shear Alfvén wave at the local Alfvén resonance, where $\omega = k_\parallel V_A$ [e.g., *Tamao*, 1965; *Uberoi*, 1972; *Chen and Hasegawa*, 1974; *Southwood*, 1974; *Hasegawa et al.*, 1983], with ω being the wave frequency and V_A being the Alfvén speed. This process can be very efficient when the fast wave propagates into a region where there is a sharp increase in the Alfvén velocity such as at the magnetopause boundary where the magnetic field increases and density decreases. Typically, the Alfvén velocity across the magnetopause increases by a factor of 10 such that an entire decade (in frequency) of wave power can be captured and localized in the boundary layer leading to massive particle transport. In the MHD description, the coupling occurs where the frequency matches the continuous spectrum and the wave becomes singular corresponding to a pileup of compressional wave energy [*Chen*, 2008].

[4] In a plasma with a 1-D inhomogeneity in the background plasma parameters along the direction perpendicular to the magnetic field, the linearized MHD equations can be expressed in terms of $\delta p_1 = B_0 \delta B_\parallel + \delta p$ and $\delta B_\perp$ by a coupled system of equations

$$-ik_\parallel\left(1 - \frac{k_\parallel^2 C_s^2}{\omega^2}\right)\delta p_1 = \left(1 + \frac{C_s^2}{V_A^2} - \frac{k_\parallel^2 C_s^2}{\omega^2}\right)B_0^2\nabla_\perp \cdot \left(\frac{\delta\mathbf{B}_\perp}{B_0}\right), \quad (1)$$

and

$$\left(\omega^2 - k_\parallel^2 V_A^2\right)B_0\delta\mathbf{B}_\perp = ik_\parallel V_A^2\nabla_\perp\delta p_1. \quad (2)$$

Singular behavior occurs at either the Alfvén resonance, $\omega^2 = k_\parallel^2 V_A^2$, or at the sound resonance, where the compressional wave couples with the Alfvén or sound wave that propagates only along the magnetic field. In higher frequency cases, the Alfvén resonance condition is modified as $\omega^2 = k_\parallel^2 V_A^2(1 - \omega^2/\Omega_i^2)^2$ because of the finite ion Larmor radius effects [*Stix*, 1992], where Ω_i is the ion gyrofrequency. The Alfvén resonance singularity can be removed by including non-MHD effects such as electron inertia or ion Larmor radius corrections in (2).

[5] Using two-fluid theory, (2) can be replaced by

$$\left[\omega^2\left(1 - \lambda_e^2\nabla_\perp^2\right) - k_\parallel^2 V_A^2\left(1 - \rho_s^2\nabla_\perp^2\right)\right]B_0\delta B_\perp = ik_\parallel V_A^2\nabla_\perp\delta p_1, \quad (3)$$

which includes electron inertial effects $\lambda_e = c/\omega_{pe}$ and electron pressure effects on the ion acoustic Larmor radius scale $\rho_s^2 = T_e/m_i\Omega_i^2$. The relative importance of electron pressure versus electron inertial effects is determined by ρ_s/λ_e, and the pressure effect is dominant if $\rho_s/\lambda_e = (4\pi nT_e/B^2)\sqrt{m_i/m_e} > 1$, which occurs when $\beta_e/2 > \sqrt{m_e/m_i} = 0.02$. Near the magnetopause, electron inertial effects are typically not important except at locations where $k_\parallel \to 0$ such as in a sheared field or reconnection geometry.

[6] Ion kinetic effects may also resolve the singularity [*Hasegawa and Chen*, 1976; *Johnson and Cheng*, 1997; *Johnson et al.*, 2001]. In this case, equation (2) is modified as

$$\left[\omega^2\hat{\mathcal{K}}_1 - k_\parallel^2 V_A^2\left(1 + \frac{T_e}{T_i}\hat{\mathcal{K}}_2\right)\right]B_0\delta B_\perp = ik_\parallel V_A^2\nabla_\perp\delta p_1, \quad (4)$$

where

$$\hat{\mathcal{K}}_1\phi(x) = \int dx' e^{ik_x(x-x')}\left[\frac{1 - \Gamma_0}{b}\right]\phi(x'), \quad (5)$$

$$\hat{\mathcal{K}}_2\phi(x) = \int dx' e^{ik_x(x-x')}\left[\frac{1 - \Gamma_0 + (Z_i'/2)b(\Gamma_0 - \Gamma_1)}{\Delta}\right]\phi(x'), \quad (6)$$

$$\Delta = -\frac{Z_e' + \frac{T_e}{T_i}Z_i'\Gamma_0}{2}, \quad (7)$$

and Z_j is the plasma dispersion function of argument $\zeta_j = \omega/\sqrt{2}k_\parallel v_j$, v_j is the thermal speed, $\Gamma_j(b) = I_j(b)e^{-b}$ with argument $b = k_\perp^2\rho_i^2$, ρ_i is the ion Larmor radius. A useful approximation may be obtained by employing the Pade approximation $(1 - \Gamma_0)/b \to 1/(1 + b)$ and high electron beta approximation, $\zeta_e \ll 1$ for which $Z_e' \to -2$, in which case the left-hand side of the equation becomes the kinetic Alfvén wave $\omega^2 = k_\parallel^2 V_A^2[b/(1 - \Gamma_0) + (T_e/T_i)b] \simeq k_\parallel^2 V_A^2[1 + (1 + T_e/T_i)k_\perp^2\rho_i^2]$ (simplified by assuming $\zeta_i \gg 1$ such that $Z_i' \to 1/\zeta_i^2 \ll 1$). Ion Landau damping may be important when $\zeta_i \sim 1$.

[7] At the resonance point, the fast wave solution is coupled to the kinetic Alfvén wave solution, and transversely polarized waves are expected to be generated and radiate away from the mode conversion location. Because the group velocity of these waves is much smaller than the compressional wave, the amplitude of the transverse fluctuations is typically much larger than the amplitude of the compressional driver, consistent with magnetopause observations [*Johnson et al.*, 2001].

[8] While analytical solutions of the above-mentioned equations have been obtained for mode conversion at the magnetopause [*Johnson and Cheng*, 1997; *Johnson et al.*, 2001], there has been no kinetic simulation addressing the mode conversion at the magnetopause. Previously, we conducted a three-dimensional (3-D) global hybrid simu-

lation of the dayside magnetosphere associated with a quasi-parallel bow shock [*Lin and Wang*, 2005]. It was found that as the compressional waves generated in the foreshock of the bow shock propagate to the magnetopause, they lead to strong surface perturbations and mode convert to shear Alfvén waves in the magnetosphere. At the magnetopause, wave energy builds up with wavelength $\lambda_\perp \sim \rho_i$, with a strong local enhancement of the parallel electric field. These waves excited in the magnetopause appear to be consistent with KAWs, but the wave mode and its formation process were difficult to identify in the global simulation. In order to identify the KAWs in the complicated global system, it is necessary to first understand the mode conversion process in a simple current sheet geometry.

[9] In this paper, we carry out a two-dimensional (2-D) hybrid simulation to examine the evolution of an incident compressional fast mode wave at the dayside magnetopause. The hybrid model solves fully kinetic equations governing the ions and a fluid model for electrons including electron pressure effects. The focus of this study will be on the identification of the mode conversion and the excitation and evolution of KAWs. For this study, we consider that locally the background magnetic field can be approximated by a slab geometry with one-dimensional (1-D) variation normal to the boundary. We further restrict these simulations to a northward IMF configuration such that the magnetic field strength increases across the current layer, but the magnetic field direction is constant. While the 3-D physics is important in the mode conversion process, we intend to address the problem in 2-D first but allow an azimuthal component of wave vector **k** perpendicular to the plane defined by the background magnetic field and the magnetopause normal. Two-dimensional calculations (in space) are sufficient to describe the linear mode conversion process in the prescribed slab configuration. Our simulation results will be compared with linear theories of mode conversion [*Hasegawa and Chen*, 1976; *Johnson and Cheng*, 1997; *Johnson et al.*, 2001]. Basic nonlinear physics of the mode conversion process will also be examined.

[10] The outline of this paper is as follows: The simulation model is described in section 2. In section 3, we present the simulation results of linear and nonlinear properties of mode conversion process. Comparison with linear theory of the mode conversion and resulting KAWs is also shown. A summary and discussion is given in section 4.

2. Simulation Model

[11] The 2-D hybrid model used in this paper was developed by *Swift* [1996] and adapted in simulations of the magnetopause current layer [*Lin and Xie*, 1997]. In the hybrid code, ions are treated as fully kinetic particles and electrons are treated as a massless fluid. Quasi-charge neutrality is assumed.

[12] The simulation is performed in the xz plane, with x being the direction normal to the magnetopause and z is the direction of wave vector tangential to the magnetopause. Initially, the magnetopause current sheet in slab geometry is assumed to be centered at $x = 0$ in the middle of the simulation domain, separating two uniform plasma regions of the magnetosheath ($x < 0$) with a high-density and low-magnetic field strength and magnetosphere ($x > 0$) with a

low-density and high-magnetic field. The initial current sheet is assumed to be a tangential discontinuity, with the normal component of magnetic field $B_x = 0$. While the direction of magnetic field can undergo an arbitrary rotation from the magnetosheath to the magnetosphere, we focus on the simplest geometry in which the magnetic fields in the magnetosheath and magnetosphere are parallel to each other, but the fields can have an arbitrary angle $\theta = \tan^{-1}(B_y/B_z)$ relative to the 2-D simulation plane, which is equivalent to allowing a nonzero, east-west, azimuthal wave vector under a northward IMF.

[13] In the calculation, the ion particles are advanced by the ion equation of motion

$$m_i \frac{d\mathbf{v}_i}{dt} = e(\mathbf{E} + \mathbf{v}_i \times \mathbf{B}), \qquad (8)$$

where $\mathbf{v}_i$ is the ion particle velocity, $\mathbf{E}$ is the electric field, $\mathbf{B}$ is the magnetic field, m_i is the ion mass, and e is the elementary charge. The electric field can be obtained from the massless electron momentum equation

$$\mathbf{E} = -\mathbf{V}_e \times \mathbf{B} - (1/Ne)\nabla P_e, \qquad (9)$$

where $\mathbf{V}_e$ and P_e are the flow velocity and thermal pressure of the electron fluid, and N is the ion number density. The electron fluid is assumed to be isothermal, with temperature

$$T_e = \text{const} \qquad (10)$$

during the evolution, and thus $\nabla P_e = T_e \nabla N$. The electron flow speed is evaluated from Ampere's law,

$$\mathbf{V}_e = \mathbf{V}_i - \frac{\nabla \times \mathbf{B}}{\mu_0 Ne}. \qquad (11)$$

The magnetic field is advanced in time from Faraday's law

$$\frac{\partial \mathbf{B}}{\partial t} = -\nabla \times \mathbf{E}. \qquad (12)$$

[14] Let the subscripts "s" and "m" represent the quantities in the magnetosheath and magnetosphere, respectively. The initial profile of the ion number density is given by

$$N(x) = \frac{1}{2}(N_m + N_s) + \frac{1}{2}(N_m - N_s)\tanh(x/D), \qquad (13)$$

where D_0 is the halfwidth of the magnetopause current sheet. The initial ion temperature T_{i0} and the electron temperature T_{e0} are assumed to be uniform everywhere, while the ions are loaded with an isotropic, Maxwellian velocity distribution. For a given magnetosheath ion beta β_{is} and T_{e0}/T_{i0}, the initial magnetic field $B(x)$ is determined by the total pressure balance

$$P(x) + B(x)^2/2\mu_0 = \text{const} \qquad (14)$$

throughout the simulation domain, where the total thermal pressure $P = P_i + P_e$. The Alfvén speed is then obtained from

$$V_A^2(x) = \frac{B(x)^2}{\mu_0 m_i N(x)} = \frac{2}{m_i}\frac{\left[B_s^2/2\mu_0 + N_s(T_i + T_e) - N(x)(T_i + T_e)\right]}{N(x)}. \qquad (15)$$

[15] In the simulation, the ion number density in the magnetosheath is chosen to be $N_s = 300$ per cell and the number density in the magnetosphere is $N_m = N_s/10 = 30$. In order to maintain a good statistical sampling of the ion distribution and a low-noise level, the actual particle numbers used for the magnetopause and the low-density magnetosphere regions are increased by a factor of 4. A smaller particle weighting is then applied correspondingly for these particles. The uniform grid size in the x direction is chosen to be $\Delta x = 0.5d_{is}$, where d_{is} is the ion skin depth in the magnetosheath, and the grid size in the z direction is $\Delta z = 2d_{is}$. For a KAW with dominant k_x satisfying $k_x\rho_i \sim$ 0.4–1 around the magnetopause and ambient magnetosheath, the grid resolution of $\Delta x = 0.5d_{is}$ is sufficient to resolve the wave structure for $\beta_{is} \sim 1$ in most of the cases to be shown. For a special case with $\beta_{is} = 0.05$, the resulting KAWs are found to have wavelengths $> 4d_{is}$, and the applied grid resolution is also adequate. The size of the simulation domain is chosen around $L_x \times L_z = 200d_{is} \times 256d_{is}$. The time step is $\Delta t = 0.05\Omega_s^{-1}$, where Ω_s is the ion gyrofrequency in the magnetosheath.

[16] Periodic boundary conditions are assumed at $z = 0$ and $z = L_z$. Free boundary conditions are used at $x = L_x/2$ on the magnetospheric side. The solar wind wave perturbations are imposed from the incoming boundary at $x = -L_x/2$ in the magnetosheath and are assumed to be a sinusoidal wave with a single frequency, $\omega = \omega_0$. For each case, the quantities k_z, $a \equiv \omega_0/(k_{\parallel 0}V_{As})$, and δV_i of the incident wave are prescribed, where $k_{\parallel 0} = k_z \cos(\theta)$ is the initial parallel wave number, V_{As} is the magnetosheath Alfvén speed, and δV_i is the wave amplitude in the flow velocity. Initially, the currents are assumed to be carried solely by ions. The imposed incident wave is assumed to satisfy the MHD fast mode dispersion relation [*Swanson*, 1989], which under the given a results in the following expression for wave propagation angle $\alpha \equiv \tan^{-1} (k_\perp/k_\parallel)$:

$$\cos^2 \alpha = \frac{a^2\left(C_s^2/V_A^2 + 1\right) - C_s^2/V_A^2}{a^4}, \qquad (16)$$

where $C_s = \sqrt{\gamma P/m_i N}$ is the sound speed, with $\gamma = 5/3$. The perturbations $\delta\mathbf{B}/B_s$, $\delta\mathbf{V}_i/V_{As}$, $\delta N/N_s$, and $\delta T_i/T_s$ are calculated from the set of the ideal MHD equations. Note that for given β_i and T_e/T_i, $C_s^2/V_A^2 = \gamma\beta_i(1 + T_e/T_i)/2$. In the simulation, it is found that the most crucial parameters to set up the initial wave are ω_0 and $k_{\parallel 0}$.

[17] In this paper, we show the results for $a = 1.5$ and 2.0 and k_z equivalent to 3–8 complete wavelengths in the z direction, which correspond to $\omega_0 \simeq 0.1\Omega_s$–$0.4\Omega_s$ and $k_0 \simeq$ 0.1/d_{is}–0.3/d_{is} (or wavelength $\simeq 20d_{is}$–$60d_{is}$). The wave amplitude is assumed to range within $\delta V_i \simeq 0.01V_{As}$ – $0.3V_{As}$, to address the basic physics of mode conversion. Note that as the wave propagates into the simulation domain from $x = -L_x/2$, it evolves self-consistently in the electromagnetic field, and the prescribed fast wave solution according to the ideal MHD may be modified to deviate from the MHD approximation because of the ion kinetic effects.

[18] In the presentation below, the time is normalized to Ω_s^{-1}. The magnetic field is expressed in units of B_s, the ion number density in units of N_s, and the temperature in units of $B_s^2/(\mu_0 N_s)$. The velocity is normalized to the magne-

tosheath Alfven speed V_{As}, and the spatial coordinates are normalized to d_{is}.

3. Simulation Results

3.1. Generation of KAWs by Mode Conversion and Comparison With Linear Theory

[19] We begin our discussion with case 1, in which $\theta = 0°$, $\beta_{is} = 0.5$, and $T_{e0}/T_{i0} = 0.4$ for the background magnetic field and plasma, and $\omega_0 = 0.392$, $a = 2.0$, and $\delta V_i = 0.04$ in the incident compressional wave. The half-width of the magnetopause current layer is $D_0 = 7.5$, equivalent to $10\rho_i$. The three thin solid lines in Figure 1 show profiles of the Alfvén speed $V_A(x)/V_{As}$ and the normalized background magnetic field strength $B(x)$ and ion density $N(x)$ as functions of x, before the magnetopause is perturbed by the incident wave. The thick solid line plots $(V_A(x)/V_{As})(1 - \omega_0^2/\Omega_i(x)^2)$. The horizontal dashed line indicates the value of $a = \omega_0/(k_{\parallel 0}V_{As})$ of the incident wave. The vertical dashed line marks the position $x = X_r \simeq 4.0$ in the magnetopause boundary, where the horizontal dashed line intersects the thick solid curve and thus the Alfvén resonance condition $\omega = k_\parallel V_A(1 - \omega_0^2/\Omega_i^2)$ is satisfied.

[20] Figure 2a depicts contours of magnetic field components B_x and B_z, ion density N, ion flow component V_{ix}, and the E_y component of electric field in partial domain around the magnetopause, obtained in case 1 at an early time $t = 80$ when the incident compressional wave just reaches the edge of the magnetopause boundary near $x = -5$ from the left. The incident wavefronts are tilted, with $k_{x0} = k_{\perp 0} = 0.262$ and $k_{z0} = k_{\parallel 0} = 0.196$. No other waves are present.

[21] At later time $t = 240$, as shown in Figure 2b for various quantities after the interaction of the incident wave with the magnetopause transition layer, reflected waves are found on the magnetosheath side, propagating across the incident waves. Meanwhile, larger-amplitude, short wavelength waves have clearly formed in the transition layer because of the interaction, where the density and magnetic field have a large gradient. In these waves, the shear components B_y and V_{iy}, E_x, and the parallel current density $J_\parallel$ are well correlated. The parallel wavelength, and thus k_z, remains nearly unchanged, while the perpendicular wavelength has decreased significantly. On the right edge of the newly formed waves, the enhanced perpendicular wave vector k_x has reversed direction from $k_x > 0$ in the incident wave to $k_x < 0$, as seen from the tilt angle of the wavefronts. These short wavelength waves appear to radiate back to the magnetosheath, leading to structures with even larger $k_\perp = k_x$ in the boundary layer. Strongly enhanced parallel electric field $E_\parallel$ is present in the resulting waves. Meanwhile, wavy perturbations in local ion temperature T_i are also observed, correlated with the variations in B_y. In the case with a larger $\delta V_i = 0.15$, to be shown later in case 4, strong enhancement in T_i is obtained around the resonance point.

[22] To illustrate the detailed structure of the short-wavelength waves generated in the magnetopause boundary layer, Figure 3a shows spatial cuts of the three magnetic field components and the parallel electric field $E_\parallel$ along x through the central region of the domain at $t = 240$, where the background B_z has a gradient, at $z \simeq 128$. In addition to the long-wavelength incident waves, coherent waves are seen to be excited apparently in B_y and $E_\parallel$, with wavelength
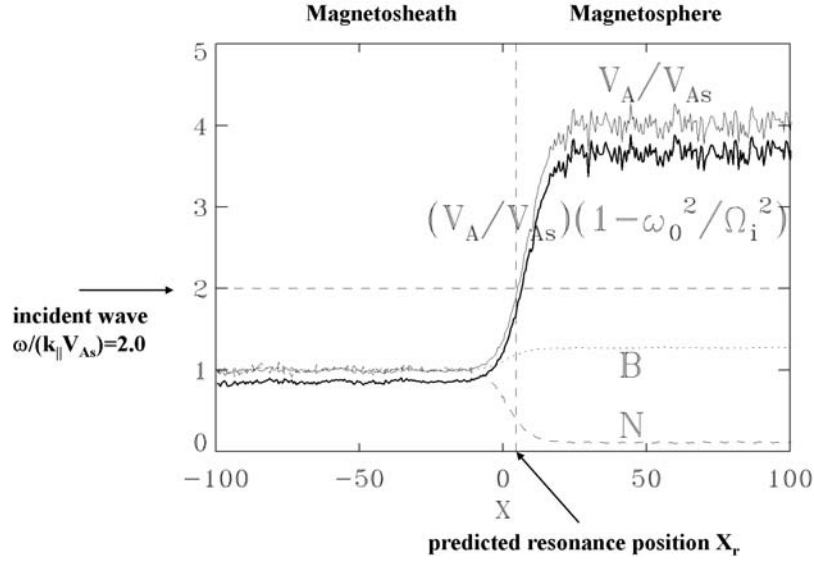
Figure 1. Three thin solid lines show Alfvén speed V_A and the normalized background $B(x)$ and $N(x)$ as functions of x across the unperturbed magnetopause in case 1. The horizontal dashed line indicates $a = \omega_0/(k_{\|0}V_{As})$ of the incident wave. The thick solid line plots $(V_A(x)/V_{As})(1 - \omega_0^2/\Omega_i(x)^2)$. The horizontal dashed line indicates the value of $a = \omega_0/(k_{\|0}V_{As})$ of the incident wave. The vertical dashed line marks the mode conversion position $x = X_r$, where the Alfvén resonance condition $\omega = k_{\|}V_A(1 - \omega_0^2/\Omega_i^2)$ is satisfied.

~ 3.15–7.35 in the x direction, corresponding to $k_\perp\rho_i \sim$ 0.4–1.0. The vertical dashed line in Figure 3a indicates the position $x = X_r = 4.0$. The strongest wave excitation is clearly coincident with the predicted Alfvén resonance position X_r, and upstream radiation of the waves is seen to some spatial extent. The excitation of these waves, at $t > 90$, is illustrated in Figure 3b, which shows the time variations of magnetic field components and $E_\|$ at $x = X_r$. The oscillations are dominated by frequency of the incident wave, $\omega = \omega_0 = 0.392$.

[23] The excitation of waves at the Alfvén resonance point is consistent with the mode conversion to KAWs. Away from the Alfvén resonance point at $x = 4.0$, waves satisfy the kinetic Alfvén wave dispersion relation. For example, near $x = 0$, $\omega^2/k_{\|}^2V_A^2 \simeq 1.78$, $k_\perp\rho_i \simeq 0.72$, and $b = k_\perp^2\rho_i^2 \simeq 0.52$. The KAW dispersion relation requires

$$\frac{\omega^2}{k_{\|}^2 V_A^2} = 1.78 \sim \left(\frac{b}{1 - \Gamma_0(b)} + \frac{T_e}{T_i}b\right) \simeq \left(1 + \left(1 + \frac{T_e}{T_i}\right)b\right)$$
$$= 1.73. \tag{17}$$

Therefore, the dispersion relation of KAWs is satisfied in these excited waves in the magnetopause. On the left side of the resonance point, the Alfvén speed is smaller. The perpendicular wavelength appears shorter with enhanced $b = k_\perp^2\rho_i^2$. The dispersion relation for KAW is again nearly satisfied.

[24] The linear growth and saturation of the KAW can be seen from the time variations of B_y and $E_\|$ for a short wavelength Fourier mode, $k_\perp\rho_i = 1.0$, shown in the left two columns of Figure 4. This mode starts to grow at $t \simeq 137$ and is saturated within a time duration of $\Delta t \sim 32.5$. The right plot of Figure 4 depicts the ratio $|\delta E_\||/|\delta E_x|$ at $x \simeq 4$ in the strong KAW, which originates from the Alfvén resonance point, with $k_\perp\rho_i \simeq 0.4$, as a function of T_{e0}/T_{i0}. A

nearly linear correlation is found, consistent with the relationship between the amplitude ratio $\delta|E_\||/\delta|E_x|$ and T_{e0}/T_{i0} for KAWs, on the basis of linear two-fluid theory with gyrokinetic closure for the ion pressure [*Hasegawa and Chen*, 1976; *Streltsov et al.*, 1998; *Cheng and Johnson*, 1999]

$$|\delta E_\|| = |\delta E_x|(k_\perp\rho_i)(k_{\|}\rho_i)(T_e/T_i)/(1 + k_\perp^2\rho_i^2). \tag{18}$$

The slope of the straight line obtained from the hybrid simulation is quite consistent with the theoretical prediction of ~ 0.03. Note that at the resonance point, $V_A \simeq 2.2V_{As}$, and thus $\beta_i \simeq \beta_s/4.8 = 0.1$. For $\omega/k_{\|}V_A \simeq 1.0$ at this point, $\zeta_i = \omega/\sqrt{2}k_{\|}v_i \sim 3.2$. Therefore, no ion Landau damping correction is necessary for (18). On the other hand, in high β plasmas, the density perturbations associated with the kinetic Alfvén wave may lead to significant magnetic field compressions. The mirror force associated with the compressions may lead to a reduction in the parallel electric field [*Cheng and Johnson*, 1999].

3.2. Wave Absorption Rate in the Mode Conversion and Comparison With Linear Theories

[25] One conclusion we can draw from case 1 is that the mode conversion from compressional waves to the KAWs takes place even for tilt angle $\theta = 0°$, i.e., without a component of $\mathbf{k}_\perp$ transverse to both the magnetic field and the magnetopause normal. This result is not expected on the basis of low-frequency theory of mode conversion [*Tamao*, 1965; *Uberoi*, 1972; *Chen and Hasegawa*, 1974; *Southwood*, 1974], in which the compressional and transverse waves are found to be completely decoupled when $\theta = 0°$.

[26] In our simulation, the mode conversion is found for cases with various angle θ of the background magnetic field,
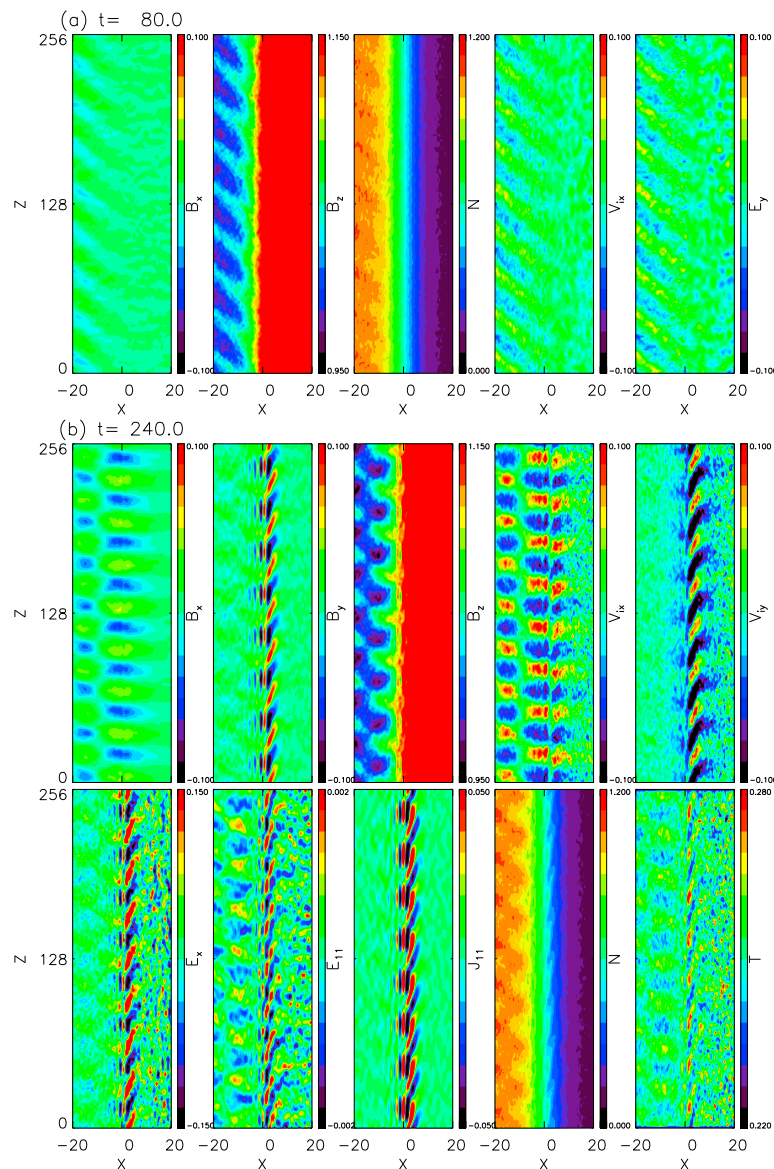
Figure 2. Contours of various quantities in partial domain around the magnetopause obtained in case 1 for (a) at an early time $t = 80$ and (b) $t = 240$. Short wavelength, coherent waves are generated by interaction between the incident wave and the magnetopause.

incident wave frequency ω_0, half-width D_0 of the initial magnetopause current layer, and the temperature ratio T_{e0}/T_{i0}. As the KAWs are excited in the boundary layer, the incident wave power is absorbed due to the Alfvén resonance. The dependence of the wave absorption rate A on various parameters is plotted in Figure 5. Because there are no transmitted waves that propagate on the magnetospheric side of the magnetopause current layer, the absorption rate can be estimated by measuring the difference between the x-components of the Poynting flux at $x = -25$ on the magnetosheath side before and after fthe mode conversion.

[27] The cross signs in the left plot of Figure 5 depict A as a function of θ obtained in the simulation for $\omega_0 = 0.147$, $a = 2.0$, $D_0 = 7.5$, $\beta_{is} = 0.5$, $T_{e0}/T_{i0} = 0.2$, and $\delta V_i = 0.04$. The absorption rate increases quickly with θ, and the wave is completely absorbed with $A \simeq 100\%$, as $\theta > 30°$, i.e., when

a moderate perpendicular wave vector exists in the plane perpendicular to **B** and **x**.

[28] The dependence of A on ω_0 obtained in the simulation is shown by the crosses in the middle plot of Figure 5, for $\theta = 0°$ and the same a, D_0, β_{is}, T_{e0}/T_{i0}, and δV_i as given above. The absorption rate A has a sensitive dependence on ω_0, increasing to a peak value of ~0.5 around $\omega_0 = 0.3$ and then decreasing at higher frequencies. It is seen that $A = 0$ for $\omega_0 < 0.1$, recovering the results based on low-frequency theories for $\theta = 0°$. However, for $\omega_0 > 0.1$ the mode conversion occurs even for cases with $\theta = 0°$. Our results indicate that finite frequency effects can remove the decoupling between the compressional and transverse waves as originally noted by *Karney et al.* [1979].

[29] In addition, the right plot of Figure 5, showing A versus D_0 under $\omega_0 = 0.147$ and $\theta = 30°$, indicates that the
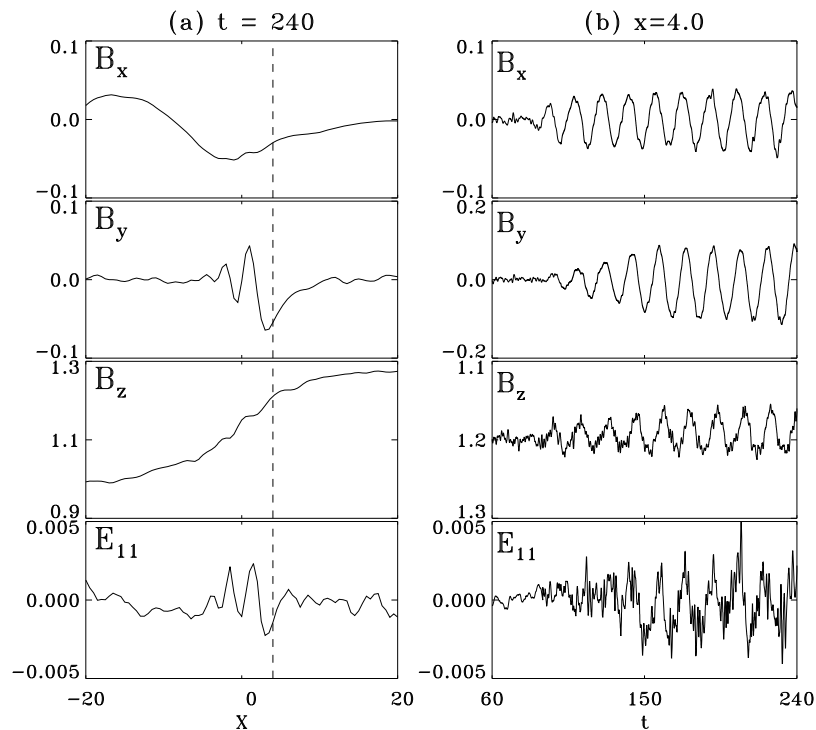
Figure 3. (a) Spatial cuts of the magnetic field components and parallel electric field at $t = 240$ along x through the central region of the domain at $z \simeq 128$ in case 1. The vertical dashed line indicates the resonance position $x = X_r = 4.0$. (b) Time variations of the quantities at $x = X_r$ show dominated frequency of the incident wave, $\omega = \omega_0 = 0.392$.

generation of KAWs and the associated absorption rate have a very weak dependence on the current sheet thickness. The rate $A \simeq 0.78$ for $D_0 = 3.0$, while $A \simeq 0.80$ for a wider current sheet with $D_0 = 7.5$, and $a \simeq 0.94$ for $D_0 = 12.5$. Note that a case with $D_0 = 1$ is also performed, but the current sheet quickly evolves to a sheet with $D_0 \simeq 3$ before the incident wave arrives. On the other hand, the absorption rate is found to be nearly independent of T_{e0}/T_{i0}, suggestive again that ion Landau damping is not playing a role for the parameter space that has been investigated.

[30] Some features of the wave absorption can be simply understood using a cold, fluid approach. In a cold plasma description, the Alfvén resonance is a singularity of the compressional wave equation. The compressional wave equation may be solved by analytic continuation around the Alfvén resonance singularity in which case there is a loss of Poynting flux at the resonance and wave energy is absorbed. Alternatively, a kinetic description of the mode conversion process involves two propagating modes (the compressional wave and the dispersive kinetic Alfvén wave), which couple
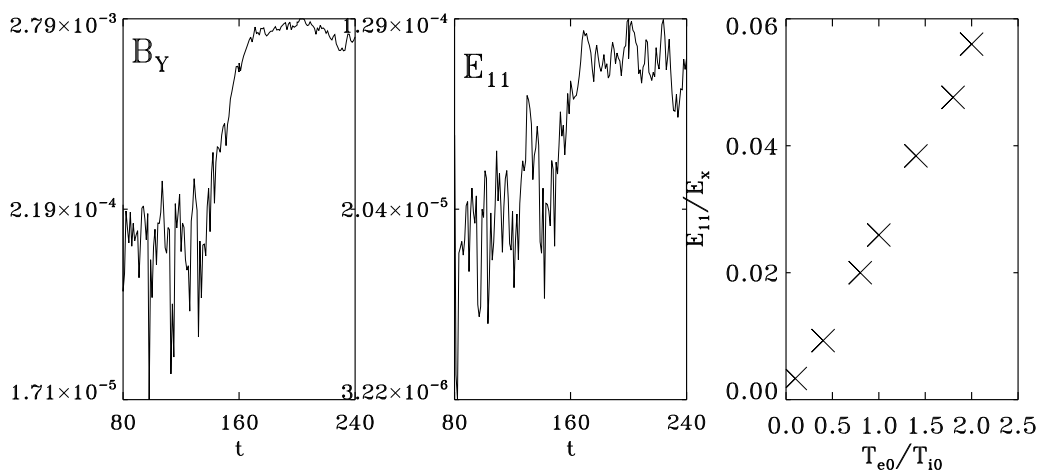

Figure 4. Time variations of (left) B_y and (middle) $E_\parallel$ for Fourier mode $k_\perp \rho_i = 1.0$ show linear growth and saturation of the KAW. (right) The ratio $|\delta E_\parallel|/|\delta E_x|$ in a strong KAW mode shows a linear correlation with T_{e0}/T_{i0}.
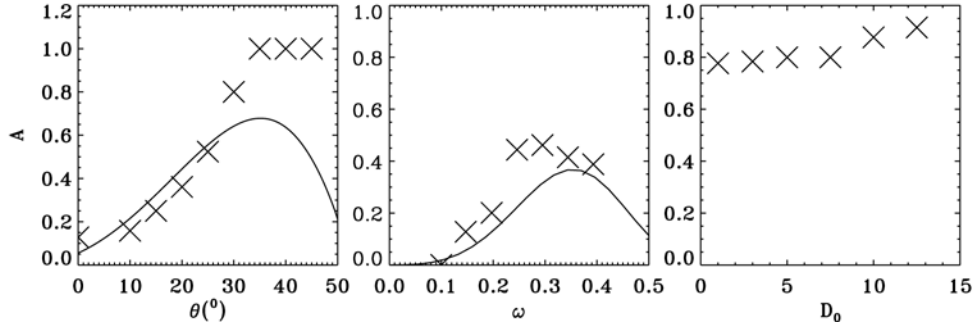
Figure 5. Cross signs show dependence of wave absorption rate A on (left) θ for $\omega_0 = 0.147$, $a = 2.0$, $D_0 = 7.5$, $\beta_{is} = 0.5$, $T_{e0}/T_{i0} = 0.2$, and $\delta V_i = 0.04$, (middle) ω_0 for $\theta = 0°$, and (right) D_0 for $\omega_0 = 0.147$ and $\theta = 30°$ obtained from the simulation. The solid curves show the corresponding results on the basis of the cold fluid theory as presented in Figure 6.

near the resonance location. Although in this case there is no wave energy loss, the amount of wave Poynting flux transferred to the mode converted kinetic Alfvén wave is basically the same as the amount of Poynting flux absorbed in the fluid description. This result is fairly typical in a cool plasma, but as the temperature of the plasma increases the Doppler shift will spread the resonance leading to a more extended coupling region. For the cases that we have examined, it appears as if the ion Landau damping may not be playing a dominant role, therefore, it would not be unusual to find our results in agreement with a cold fluid result.

[31] To proceed, we consider a cold plasma magnetopause slab model with equilibrium plasma variation in the x-direction as in the simulation model. The perturbed fields are assumed to vary as $\phi = \Phi(x)\exp[i(k_v v + k_\parallel \zeta - \omega t)]$ where the coordinates (x, v, ζ) are a set of Cartesian coordinates with ζ along the magnetic field direction (not to be confused with the z coordinate in the hybrid simulations) and v in the $\hat{\mathbf{b}} \times \hat{x}$ direction. In terms of the coordinate system of the simulations, $k_z^2 = k_v^2 + k_\parallel^2$, $k_\parallel = k_z \cos\theta$, and $\theta = \tan^{-1}(k_v/k_\parallel)$. Wave propagation in the cold, fluid model can be described by Mawell's equations combined with fluid equations for ions and electrons. Using the form of perturbations described above, a simple set of wave equations [*Swanson*, 1989] can be obtained by ignoring electron inertial effects and background gradients related to diamagnetic drift and density compressions,

$$\frac{c}{\omega} \frac{d\Phi}{dx} = M\Phi, \qquad (19)$$

where

$$\Phi = \begin{pmatrix} E_v \\ \dfrac{c}{\omega} \dfrac{dE_v}{dx} - i n_v E_x \end{pmatrix} \qquad (20)$$

and

$$M = \begin{pmatrix} \dfrac{n_v D}{n_\parallel^2 - S} & 1 + \dfrac{n_v^2}{n_\parallel^2 - S} \\ \dfrac{\left(n_\parallel^2 - R\right)\left(n_\parallel^2 - L\right)}{n_\parallel^2 - S} & -\dfrac{n_v D}{n_\parallel^2 - S} \end{pmatrix}, \qquad (21)$$

with $n = kc/\omega$ and R, L, S, and D being the Stix functions. In general, these equations have a singularity at the location where $n_\parallel^2 = S$. For low frequency, this is the Alfvén resonance ($\omega = k_\parallel V_A$) and for higher frequency it is the so-called perpendicular ion cyclotron resonance ($\omega = k_\parallel V_A(1 - (\omega/\Omega_{ci})^2)$) [*Karney et al.*, 1979; *Winglee*, 1982; *Stix*, 1992].

[32] The low-frequency limit of these equations is given by $R = L = S = c^2/V_A^2$ and $D/S = \mathcal{O}(\omega/\Omega_i)$ such that we obtain

$$\epsilon \frac{d}{dx}\left(\frac{1}{\epsilon} \frac{d\Phi_1}{dx}\right) = \left(\left(k_\parallel^2 + k_v^2\right) - \omega^2/V_A^2\right)\Phi_1 \qquad (22)$$

with a resonance condition at $\epsilon(x) = 0$ where

$$\epsilon = 1 - \left(\frac{\omega^2}{k_\parallel^2 V_A^2}\right). \qquad (23)$$

In the low-frequency limit when $k_v, \omega \to 0$,

$$M \to \begin{pmatrix} 0 & 1 \\ n_\parallel^2 - c^2/V_A^2 & 0 \end{pmatrix} \qquad (24)$$

and the singularity disappears from the equations as in the MHD approximation. However, when $\omega \sim \Omega_i$, the equations are singular even when $k_v = 0$ ($\theta = 0$).

[33] The higher-frequency (ω/Ω_i) effects on magnetosonic mode conversion described by (21) were first discussed by *Karney et al.* [1979], where it was recognized that there is a cutoff-resonance-cutoff triplet (allowing a small region of propagation on the high Alfvén velocity side of the resonance). *Karney et al.* [1979] estimated the fractional power absorbed using an approximate version of (21) (using linearized spatial dependence in the coefficients) with the method of matched asymptotic expansion consistent with the approximation of small $k_v/k_\parallel = \tan\theta \ll (k_z L_n)^{1/3}$. Although they found significant absorption even when $k_v = 0$, they emphasized that it would be possible to control parameters so as to minimize such damping at higher frequency. By retaining additional terms proportional to $k_v \omega/\Omega$, *Winglee* [1982] extended the result to larger wavelength using matched asymptotic expansions, which provided a better estimate of the peak absorption.

[34] *Majeski et al.* [1994] later examined mode conversion from magnetosonic waves to the slow ion Bernstein wave
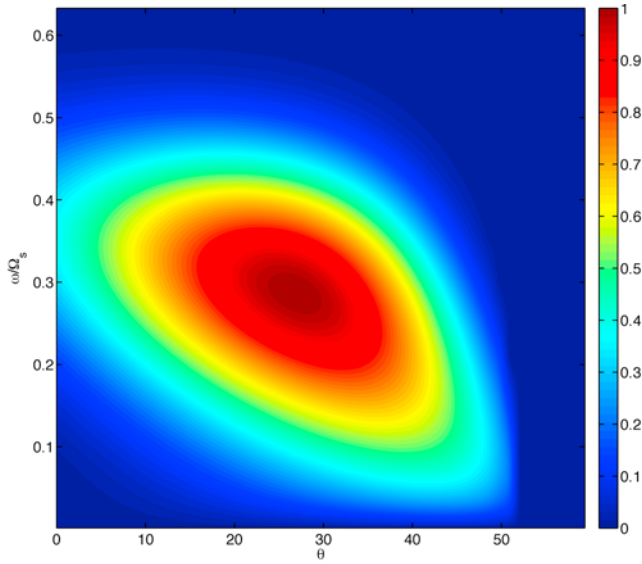
Figure 6. Theoretical solutions of wave absorption rate A as a function of frequency and θ on the basis of a cold fluid description.

for the case of the ion-ion hybrid resonance and obtained the following equation using (21) in the case with multiple ion species with the approximation $k_v = 0$:

$$\frac{d^2\Phi}{dx^2} = \frac{c^2}{\omega^2} \frac{\left(n_\parallel^2 - L\right)\left(n_\parallel^2 - R\right)}{\left(n_\parallel^2 - S\right)} \Phi. \qquad (25)$$

The dispersion relation for this case is topologically equivalent to the perpendicular Alfvén-ion cyclotron resonance with a cutoff-resonance-cutoff triplet when the wave propagates from low field to high field. This work focused on the importance of the high-field cutoff and demonstrated that wave interference results in a standing wave pattern between the resonance and high-field cutoff leading to an oscillatory behavior of the absorption coefficients. *Ram and Bers* [1996] examined the ion-ion hybrid resonance in further detail, suggesting that this resonator effect could lead to 100% mode conversion efficiency.

[35] To investigate wave absorption in our simulations, we solve (19) and (21) for the same magnetopause background profile prescribed in section 2 without making any local approximations for the coefficients. In order to isolate the dependence of the absorption on ω and θ from the dependence on background gradient, we fix the mode conversion location to be at the center of the current layer by prescribing that $n_\parallel^2 = S$ for a given frequency (i.e., $n_\parallel^2 = S(\omega, x = 0)$), and we then compute the absorption as a function of k_v or equivalently $\theta = \tan^{-1}(k_v/k_\parallel)$ for a given frequency. Note that θ is identical to the tilt angle used in the hybrid simulations.

[36] To obtain the wave absorption, we solve the wave equations subject to suitable wavescattering boundary conditions, i.e., there is an incoming wave with unit Poynting flux from the magnetosheath and no incoming wave from the magnetosphere. These boundary conditions are adequate to determine the Poynting fluxes of the reflected wave, R,

and the transmitted wave, T. Generally, for most parameters the compressional wave decays on the magnetospheric side of the resonance so that there is no transmitted wave. The wave absorption is obtained from the lost fraction of wave energy $A = 1 - R - T$. The wave solution is obtained by integrating the differential equation on a contour that is deformed in the complex plane around the singularity [*Johnson*, 1992]. Two linearly independent solutions are obtained and superposed in such a way as to satisfy the boundary conditions above. The wave solutions generally consist of a wave propagating from the magnetosheath to a cutoff and decaying into a resonance location. The wave sometimes has a region of propagation beyond the resonance before it is cutoff again and decays into the magnetosphere.

[37] The solutions are shown in Figure 6 as a function of frequency and θ. At low frequency, the MHD result is obtained with a maximum absorption around 10%. For $\theta = 0$ appreciable absorption occurs for $\omega/\Omega_i > 0.1$ maximizing around $\omega/\Omega_i = 0.3$. Above $\omega/\Omega_i = 0.5$, there is no absorption as well as beyond 50°. The reduction in absorption typically occurs as the cutoff retreats from the magnetopause toward the magnetosheath leaving an extended damping region such that the wave cannot leak to the resonance. Above $\omega/\Omega_i = 0.5$, the compressional wave cannot propagate in the sheath. Unlike the Budden tunneling problem [*Budden*, 1961], which has a maximum of 25% absorption for waves that approach a resonance through an evanescent region, the absorption maximizes at $\theta \sim 25°$ and $\omega/\Omega_i \sim 0.3$ with nearly 100% efficiency. The reason for the difference from Budden tunneling is that the wave is also cutoff on the magnetospheric side of the resonance so that the transmitted wave energy is reflected back into the resonance where it can be totally absorbed. In this case, wave interference effects do not lead to oscillations in the absorption coefficient because the distance between the resonance and the high-field cutoff is small compared with the wavelength.

[38] The theoretical absorption rates are also shown by solid lines in the left and middle plots in Figure 5, for comparison with the simulation results. The monotonic increase of A at $\theta < 35°$ obtained in the simulation is rather consistent with the theory, and the peak of A near $\theta = 35°$ also agrees with the theory. Moreover, the overall trend of the simulated A as a function of ω is consistent with the theoretical curve, which is based on a cold plasma assumption.

[39] It is also interesting to consider whether it is reasonable to neglect terms related to the diamagnetic drift (background pressure gradients), which can be appreciable at the high-β magnetopause. These effects become important when the drift frequency, $\omega_d = \mathbf{k} \cdot \mathbf{b} \times \nabla \log P/\Omega_i$, becomes the order of the wave frequency, $\omega_d/\omega \sim k_y v_i (\rho_i/D_0)/k_\parallel V_A \sim \tan\theta \sqrt{\beta/2}(\rho_i/D_0) \sim 1$. For $\theta < 50°$, $\beta = 1$, and $\rho_i/D_0 \sim 0.1$, we find that $\omega_d/\omega < 0.08$, which justifies neglecting the perturbed currents related to gradients in the background magnetic field and pressure.

3.3. Decay of Compressional and Transverse Waves in the Magnetosphere

[40] As predicted by the linear theory [*Hasegawa and Chen*, 1976], the waves decay on the magnetospheric side of the Alfvén resonance point. Wave power for each of the magnetic field components for the $\omega = \omega_0$ mode is shown in
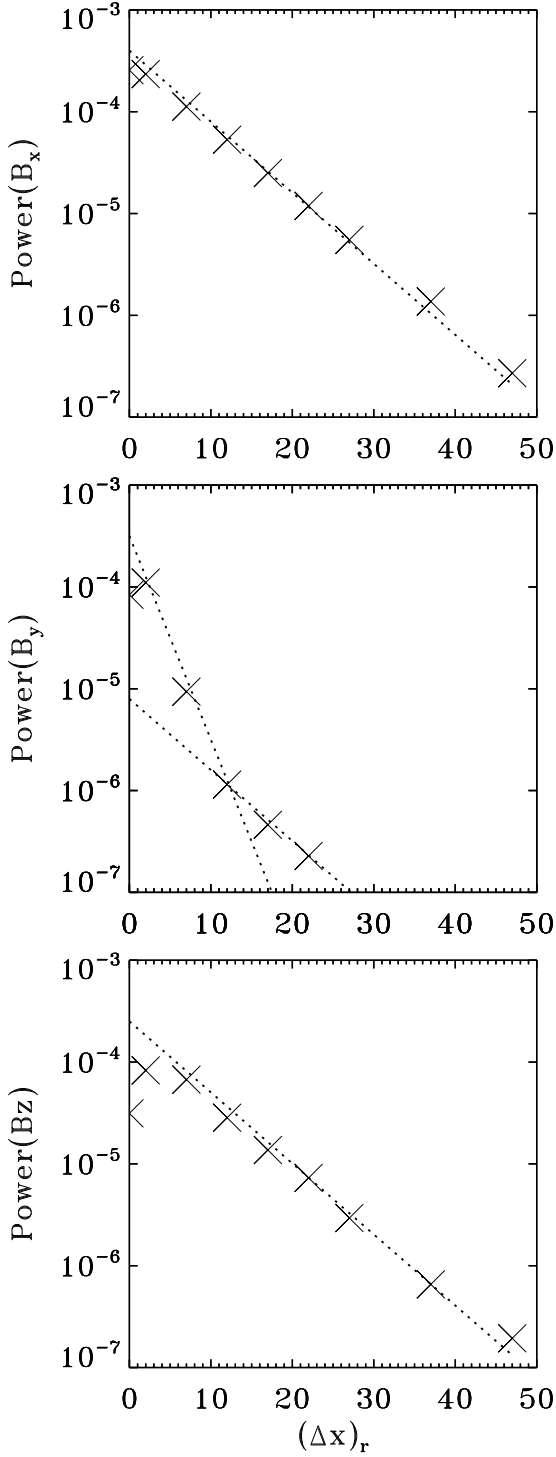
Figure 7. Wave powers of magnetic field components for the $\omega = \omega_0$ mode as a function of distance $(\Delta x)_r \equiv x - X_r$, shown by crosses obtained from case 2. The dashed lines represent exponential fits to the power variations.

Figure 7 as a function of distance $(\Delta x)_r \equiv x - X_r$ (indicated by the symbol "x") for case 2 with $\theta = 30°$, $\beta_{is} = 0.5$, $T_{e0}/T_{i0} = 0.2$, $\omega_0 = 0.149$, $a = 2.0$, $\delta V_i = 0.1$, and $D_0 = 7.5$, where the resonance point $X_r = 3.0$. The parallel wave number $k_{\|0} = k_{z0} \cos 30° = 0.074$. The dashed lines represent exponential fits to the power variations, $\sim \exp[-(\Delta x)_r/l]$. The exponential

decay begins at about $(\Delta x)_r = 2$, a distance of $2d_{is}$ on the right side of the resonance point. On basis of the exponential fits of the wave powers $|B_x(\omega_0)|^2$ and $|B_z(\omega_0)|^2$, the decays of $|B_x(\omega_0)|$ and $|B_z(\omega_0)|$, dominated by the compressional modes, are found to correspond to an e-folding distance of $l = 12.4$. On the other hand, the exponential decay length of the compressional wave can be estimated theoretically from $l^2 = -1/k_x^2$. From the fast mode dispersion relation,

$$\omega^2 \simeq k^2(V_A^2 + C_S^2) - k_{\|}^2 C_S^2, \tag{26}$$

which results in

$$k_x^2 = \omega^2/(V_A^2 + C_S^2) - k_z^2 \sin^2\theta - k_{\|}^2 V_A^2/(V_A^2 + C_S^2). \tag{27}$$

For the fast mode with $\theta = 30°$, and $\beta = \beta_i + \beta_e = 0.15$ around the resonance point in case 2, and noting $k_z = k_{\|}/\cos\theta$ and $(1 + C_S^2/V_A^2) = (1 + \gamma\beta/2)$, we have

$$l \simeq (1/k_{\|})/\sqrt{\tan^2\theta + 1/\left(1 + \gamma\frac{\beta}{2}\right) - \omega^2/k_{\|}^2 V_A^2\left(1 + \gamma\frac{\beta}{2}\right)}$$

$$= (1/k_{\|})\sqrt{0.33 + 0.89\left(1 - \omega^2/k_{\|}^2 V_A^2\right)}. \tag{28}$$

At the decay location, the perturbed Alfvén speed is estimated to be $\delta V_A/V_A \simeq 0.25$, which leads to $l \simeq 15.3$. Therefore, the decay distance obtained from the simulation is roughly that from the theoretical Wentzel-Kramers-Brillouin approximation.

[41] The decay of the $|B_y(\omega_0)|^2$ wave power is different from the decay of the $|B_x(\omega_0)|^2$ and $|B_z(\omega_0)|^2$ wave power in that it appears to possess two scales: a steep decay in $|B_y|$ followed by a slower exponential decay with $l = 12.4$. The steeper decay in $|B_y|$ is due to the combined effects of KAW excited at the resonance point and compressional mode, while the slower part is consistent with that of B_x and B_z, corresponding to the decay of the compressional mode. For the KAW, $k_x \gg k_y' \equiv k_z \tan\theta$, and thus the perturbation in B_y is dominant over that in B_x and B_z. Note that in this case with $\theta \neq 0°$, the compressional mode has a finite polarization in B_y. On basis of the the linear theory [*Hasegawa and Chen*, 1976], the KAW in the Airy region decays with a steeper $\exp(-2z^{3/2}/3)$, where $z = \Delta x/(\rho_i^2 D_0)^{1/3}$, which is not quite exponential.

3.4. Nonlinear Effects: Generation of Harmonics in the Mode Conversion

[42] At the magnetopause, it is usually the case that magnetic field fluctuations are large, $\delta B_\perp/B_0 \sim 1$, such that nonlinear effects should be considered [e.g., *Rezeau et al.*, 1986; *Song et al.*, 1993a, 1993b; *Phan et al.*, 1996b]. To examine nonlinear effects on the mode conversion process, we increase the amplitude of the driver in a systematic manner (controlled by the velocity perturbation, δV_i) and examine the resulting wave structure and spectral properties. We find a number of interesting nonlinear properties: passive generation of harmonics for weak nonlinear driving wave breaking in the upstream compressional wave evidenced by upstream generation of nonlinear harmonics, and general broadening of the wave spectrum such that there is a
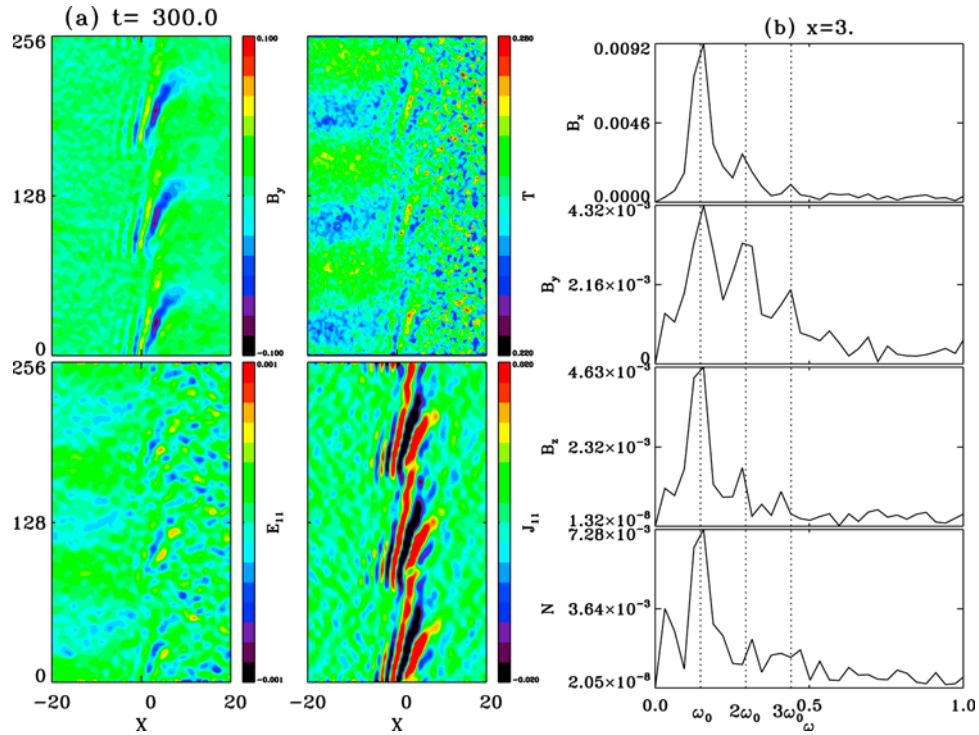
Figure 8. (a) Contours of various quantities and (b) frequency spectra of various quantities at the resonance point $x = X_r = 3.0$ obtained from case 3. The three vertical dashed lines in Figure 8b mark $\omega = \omega_0$, $2\omega_0$, and $3\omega_0$.

broadening of the resonant region to encompass the entire Alfvén-cyclotron continuum across the magnetopause.

[43] For weak nonlinear driving, we find that in addition to the primary mode with $\omega = \omega_0$, multiple harmonics of ω_0 are generated in the region of mode conversion. Figure 8a shows the 2-D contours of various quantities in case 3, which is similar to case 2 except for $\theta = 0°$ and $\delta V_i = 0.04$. The incident fast wave has only three full wavelengths within the domain length L_z, with $k_{x0} = 0.102$, $k_{\|0} = k_{z0} = 0.074$, and thus a low frequency of $\omega_0 = 0.149$ for $a = 2.0$. Note that this incident wave is close to being in the MHD regime. Again, short wavelength KAWs are present at the center of the domain because of the mode conversion from the incident compressional wave.

[44] By plotting the Fourier spectra in ω space at the resonance point $x = X_r = 3.0$, we show in Figure 8b the frequency spectra of B_x, B_y, B_z, and ion density N. The three vertical dashed lines in Figure 8b mark the three harmonics at $\omega = \omega_0$, $2\omega_0$, and $3\omega_0$. Not only the primary harmonic mode with $\omega = \omega_0$ is present, higher order harmonics are also excited in all the transverse and compressional field components, as well as in the density. The powers of these modes decrease with the order of the harmonics, with the primary harmonic mode $\omega = \omega_0$ being the strongest and dominant. Correspondingly, harmonics of the incident $k_{\|0}$ also appear.

[45] Note that the weak peak of power near $\omega = 0$ is due to the slow motion of the magnetopause boundary layer as the incident wave continuously impinges upon it. No $\omega = 0$ mode is found in the simulation. The source of the harmonic generation in case 3 is within the local region of the mode conversion in the magnetopause boundary. Subsequently,

multiple harmonics are also seen in the reflected wave spectrum on the magnetosheath side.

[46] Such nonlinear harmonic mode generation is seen at all amplitudes of incident waves. The top and bottom plots in Figure 9 show the decay of $|B_x(\omega)|^2$ with distance $(\Delta x)_r$ for the primary ($\omega = \omega_0$) and secondary ($\omega = 2\omega_0$) harmonic modes, respectively, for cases similar to case 3 but with three different incident wave amplitudes $\delta V_i = 0.04$ (plotted with ×s), 0.1 (stars), and 0.15 (squares). For both modes, the decay constants remain nearly unchanged for the different wave amplitudes. The decay of the higher harmonic modes, however, is much faster than that of the primary mode. The decay constant $l = 8.4$ for $|B_x(\omega)|$ in the second harmonic mode, while $l = 12.4$ in the primary mode, similar to those in Figure 6. Let $k_{\|} = 2k_{\|0}$, the theoretical decay length obtained from (28) for the second harmonic mode is 7.6, again close to $l = 8.4$ measured in the simulation. This linear decay of the individual modes suggests that the generation of the harmonics occurs primarily in the region of linear mode conversion (the dissipative region for an MHD description) and that the harmonics radiate away from the resonance regions as uncoupled linear modes.

[47] Theoretically, as the amplitude of the driver wave is increased, it is expected that the wave should, indeed, first become nonlinear near the resonance location, where the wave solution is singular in MHD and has large amplitude in a kinetic description consistent with a small group velocity across the magnetic field. *Dmitrienko* [1997], *Clack et al.* [2009], and *Clack and Ballai* [2009] have discussed the weakly nonlinear interaction of fast magnetosonic waves in a 1-D planar plasma using an MHD description. They derived a hierarchy of equations considering the MHD
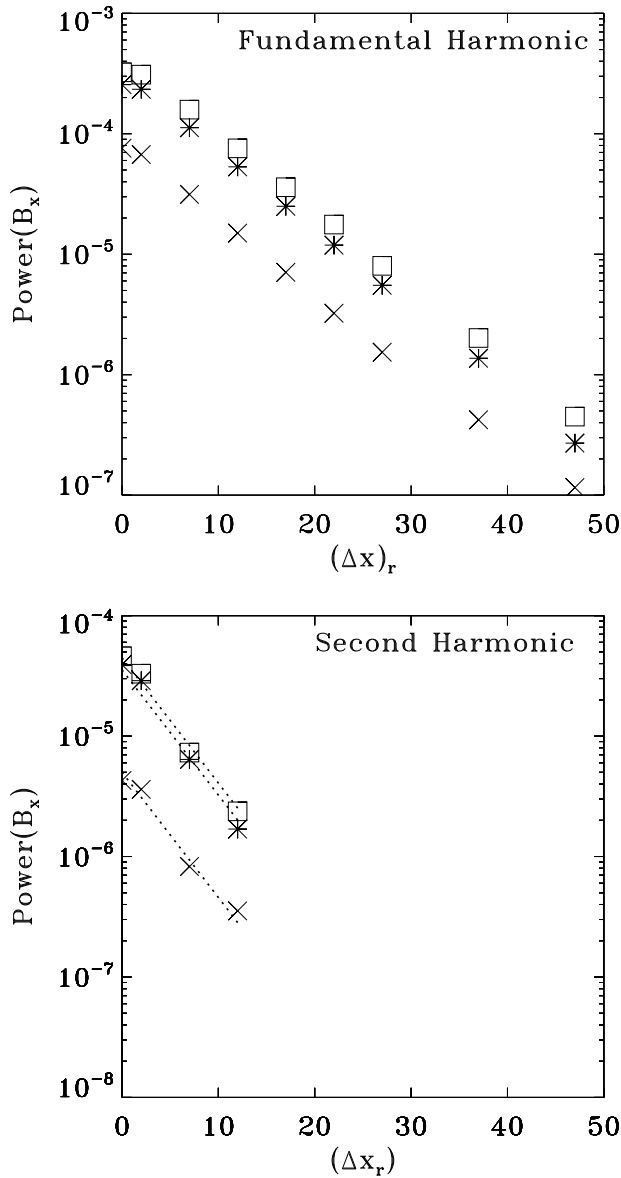
Figure 9. Decay of $|B_x(\omega)|^2$ with distance $(\Delta x)_r$ for the (top) primary $(\omega = \omega_0)$ and (bottom) secondary $(\omega = 2\omega_0)$ harmonic modes for cases with incident wave amplitude $\delta V_i = 0.04$ (crosses), 0.1 (stars), and 0.15 (squares).

singular variables B_y and V_y as large and the other components as higher order. Based on this hierarchy, they found that the governing equation for the second-order terms was the same as for the first-order terms in the singular region with the addition of nonlinear terms involving products of first-order terms. However, at the resonant surface, the driving forces associated with perpendicular velocity and magnetic field nonlinearly cancel each other [*Dmitrienko*, 1997; *Clack et al.*, 2009], suggesting that nonlinear effects would mostly lead to radiation of second-order compressional waves [*Clack et al.*, 2009]. However, in a kinetic description the resonant region is broadened by wave dispersion, such that the large-amplitude second-order nonlinear perpendicular magnetic field and velocity response associated with the kinetic Alfvén wave does not cancel in the region of small-

scale structure, leading to the generation of second-order harmonic structure in the dispersive kinetic Alfvén waves seen near resonance.

[48] Likewise, the third-order equation involves nonlinear terms that are products of first-order and second-order terms and so forth. Consequently, if the first order solution has the typical behavior discussed previously, $\delta B_\perp^{(1)} = g^{(1)}(x) \exp(i(kz - \omega t))$, products of the first-order solutions would behave like $\exp(2i(kz - \omega t))$ implying that $\delta B_\perp^{(2)} = g^{(2)}(x) \exp(2i(kz - \omega t))$ with amplitude that scales with the square of the driver amplitude. Similarly the nth harmonic would scale with the nth power of the amplitude. These properties are seen qualitatively in Figure 7b in that harmonics are generated having decreasing amplitude with increasing harmonic order.

[49] For larger frequency and/or amplitude of the compressional wave driver (or if the ion β_i is small), harmonics of ω_0 can be generated in the incident compressional wave before it reaches the magnetopause, because of nonlinear steepening. The left column of Figure 10a shows the Fourier spectra of the incident wave in case 4, taken at $x = -65.0$ on the magnetosheath side during early time interval of $t = 0$–120 before the arrival of the reflected waves from the mode conversion region. In this case, $\theta = 0°$, $D_0 = 7.5$, $k_{\|0} = 0.196$, $k_{\perp 0} = 0.326$, the frequency $\omega_0 = 0.392$, which is much larger than that in case 3, and the wave amplitude is also larger with $\delta V_i = 0.15$. A cold plasma with $\beta_i = 0.05$ and $T_e = T_i$ is assumed. Multiple harmonics at $\omega = 2\omega_0$ and $3\omega_0$ are seen in the incident compressional component B_z, in addition to the primary $\omega = \omega_0$. Meanwhile, the incident wave has steepened from the initially presumed sinusoidal structure. The steepened wave is of a nondispersive nature, with all the harmonic modes still satisfying the same fast mode dispersion relation. The harmonics of $\mathbf{k_0}$ are generated correspondingly. Different from the results in Figure 8b, the wave powers do not necessarily decrease with the order of harmonics.

[50] As the wave steepens, the wave power is also present in the transverse component B_y, whose oscillation modes appear not only at the harmonics of ω_0 but also in between the harmonics. The nonlinear self-evolution of the incident wave has resulted in the formation of weak transverse Alfvén modes in the incident wave.

[51] The middle and right columns of Figure 10a depict the power spectra analyzed for data from the entire simulation run of case 4 from $t = 0$–200, at $x = 5.0$ inside the magnetopause boundary and $x = 35$ on the magnetosheath side, respectively. Harmonics are again seen in the mode conversion region, because of the mode conversion from multiple incident modes shown in the left column of Figure 10a. Unlike the results in Figure 8b for case 3, in which no multiple harmonics exist in the incident wave, the powers of harmonics do not decrease with the harmonic order. The harmonics obtained in the right column has included the contributions from both the incident and returned waves.

[52] Spatial structures of various quantities in the xz plane obtained in case 4 are shown in Figure 10b. Around the Alfvén resonance point, where waves in V_{iy} and $J_\|$ are present, the ion temperature peaks strongly, with T_i enhanced by a factor of 2, correlated with the increases in the ion density. The heating is seen predominantly in the perpendicular directions. Moreover, strong momentum
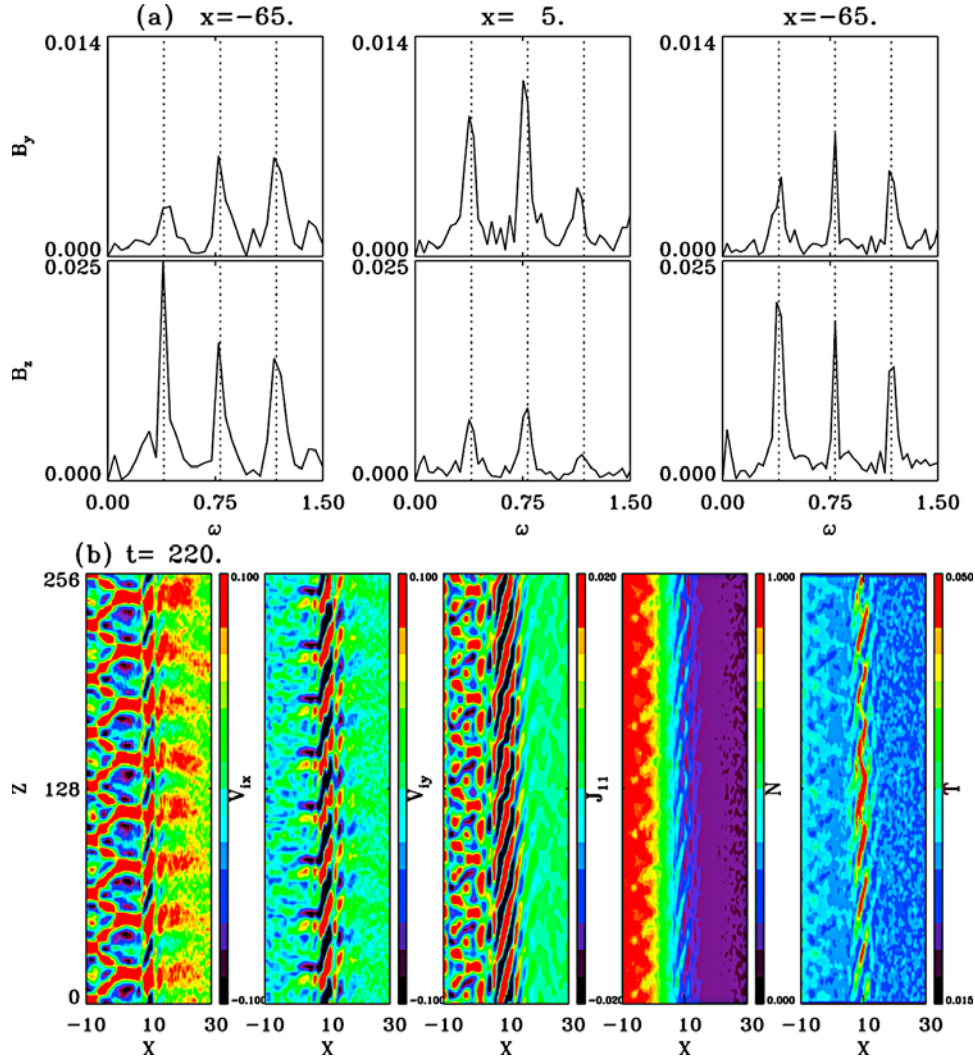
Figure 10. Simulation results of case 4. (a) Fourier spectra of (left) the incident wave during early times at $x = -65.0$ in the magnetosheath and resulting waves at (middle) $x = X_r = 5.0$ in the magnetopause boundary and (right) $x = 35$ on the magnetosheath side during the entire simulation time. (b) Spatial structures of various quantities in the xz plane.

transport to the magnetosphere is seen in the ion bulk flow component V_{ix}. Note that the larger amplitude of the incident wave has also caused the magnetopause to gradually shift to the right. According to the linear theory [*Hasegawa and Chen*, 1976], the perpendicular wavelength of the KAWs generated from the mode conversion process is related to ρ_i in the magnetosheath and D_0 of the magnetopause scale length as $\lambda_\perp \sim (\rho_i^2 D_0)^{1/3}$ near the resonance location and $\lambda_\perp \sim \rho_i$ away from the resonance, which results in $k_\perp \rho_i$ ranging from $\sim (\rho_i/D_0)^{1/3}$ to ~ 1. Colder magnetosheath ions would be consistent with shorter wavelengths for the KAW solutions with respect to d_i, but smaller $k_\perp \rho_i$. In case 4 with $\beta_i = 0.05$, the wavelength $\lambda_\perp$ of the resulting KAW at the resonance point is indeed smaller than that in case 1 with $\beta_i = 0.5$ by a factor of $(\rho_i^2/\rho_i'^2)^{1/3} = (T_i/T_i')^{1/3}(\Omega_i'/\Omega_i)^{2/3} \sim (2\beta_i/\beta_i')^{1/3}(B'/B)^{2/3} \sim (2 \times 0.1)^{1/3}(1.25/1.05)^{2/3} \sim 0.7$, where the quantities with and without the prime indicate those of case 1 and case 4, respectively. Note that a factor of 2 in the temperate enhancement at the resonance point in case 4 has been considered in the estimate.

3.5. Nonlinear Effects: Broadening of the Mode Conversion Region

[53] At low frequency, the appearance of paired harmonics would not alter the resonance location for the harmonic waves because $\omega_0/k_{\|0} = 2\omega_0/2k_{\|0} = \ldots = n\omega/nk_{\|0} = V_A$, so that the nonlinear resonant wave structure should be localized at the primary resonance. Moreover, because all the harmonics have the same phase speed along the field, it might be expected that there would be little wave breaking for Alfvén waves propagating along the field. On the other hand, as discussed previously, higher frequency effects on the Alfvén resonance condition imply that the resonance occurs at $\omega = k_\| V_A(1 - \omega^2/\Omega_i^2)$. In this case, higher harmonics would require a larger V_A to satisfy the resonance condition, and the nonlinear wave structure should shift toward the region of increasing V_A. In this manner, the generation of harmonics near the fundamental resonance could lead to a spreading of the resonant wave structure in the direction of increasing V_A. However, the resonance
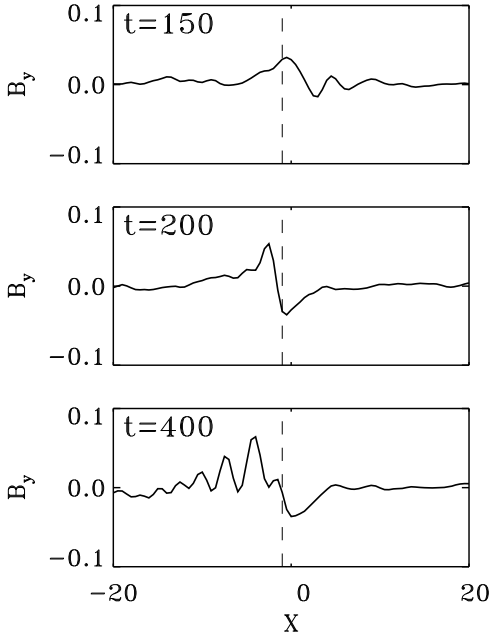
Figure 11. Spatial cuts of B_y as a function of x around $z = 128$ at $t = 150$, 200, and 400 show the broadening of the Alfvén resonance region in case 5. The vertical dashed lines indicate the resonance point at $x = X_{r1}$.

condition itself may only be satisfied for a limited range of frequency, which satisfies $n_\parallel^2 = S$ between the primary resonance and the maximum Alfvén velocity on the right side of the domain. The harmonic number n is bounded by the relation

$$n^2 < \left(\frac{\Omega_i}{\omega_0}\right)^2 - \frac{V_{A0}}{V_{A\max}}\left[\left(\frac{\Omega_i}{\omega_0}\right)^2 - 1\right] \qquad (29)$$

so that more harmonics would be allowed if ω_0/Ω_i is smaller and/or if the Alfvén velocity increases significantly from the resonance location to the magnetosphere. In the simulations, the broadening of the resonance is more pronounced at lower frequency, consistent with this argument.

[54] In the simulations, it also appears that nonlinear wave-wave interaction results in (a) broadening of the spectral bandwidth in ω and (b) the appearance of large amplitude waves within the Alfvén continuum. Neither the broadened modes nor the continuum modes appear as harmonics of the primary wave driver. The appearance of the continuum modes is most obviously seen in case 5 shown below, in which $a = 1.5$, $\omega_0 = 0.294$, $\theta = 0°$, $\beta_{is} = 0.5$, $T_{e0}/T_{i0} = 0.4$, $\delta V_i = 0.04$, $D_0 = 7.5$, and $k_{\parallel 0} = 0.196$.

[55] Figure 11 shows the spatial structure of B_y as a function of x around $z = 128$ at $t = 150$, 200, and 400. The vertical dashed lines indicate the resonance point at $x = X_r = -1.0$. The broadening of the Alfvén resonance region is evident at $t = 150$, when the wavy structure of B_y is seen throughout the region from $x = X_r$ to $x \simeq 9$ on its right, with a larger amplitude at $x = X_r$. At $t = 200$, the waves at $x = X_{r1}$ become predominant, while weaker perturbations are still seen on its right. At $t = 400$, the peak at $x = X_r$ has obviously shifted to the right, and the perturbations occupy a broad

area. Again, strong KAWs with larger $k_\perp$ also radiate into the magnetosheath on the left side of $x = X_r$.

[56] A close examination shows that on the right side of the resonance point $x = X_r$, the wave spectral width in ω is significantly broadened in the way that modes with frequencies other than ω_0 are also excited at $k = k_{\parallel 0}$. Figure 12 depicts the powers of B_x and B_y in the $k_\parallel$-ω plane at $x = X_r = -1.0$ and $x = 9.0$. Discrete harmonic modes $(k_{\parallel 0}, \omega_0)$ and $(2k_{\parallel 0}, 2\omega_0)$ are present clearly in all the three field components (B_z not shown) at the resonance point $x = -1.0$. At $x = 9.0$ on the magnetospheric side, however, broad spectra with $\Delta\omega \simeq 0.9\omega_0$ appear predominantly in B_x and B_y at $k_\parallel = k_{\parallel 0}$, in addition to the mode near $(k_{\parallel 0}, \omega_0)$. Continuous spectral curves are also shown across the $k_\parallel$-ω space, which are found to be the normal modes that also exist under a random perturbation of the boundary layer without the incident coherent waves and in principle could also be excited by the numerical noise. In fact, the dominant mode in B_y appears at $(k_{\parallel 0}, 1.9\omega_0)$, coincident with the curvy continuous spectrum at $k_{\parallel 0}$, whereas the power in B_x is still dominated by the primary $(k_{\parallel 0}, \omega_0)$.

[57] In addition to the shifted resonance locations due to the presence of harmonic modes, the broadening of the mode conversion region shown in Figure 11 may also be associated with the broadening of ω spectrum at $k_\parallel = k_{\parallel 0}$. Because of the presence of compressional wave power in the broad band of wave frequency, the Alfvén resonance condition can be satisfied in a broad area of the density gradient layer, although the waves are weaker beyond the primary resonance point $x = X_r$. Such an effect implies that transport processes can occur over a wider region encompassing most of the magnetopause. Consequently, it is expected that diffusive processes would be more efficient in that they operate over a wider spatial region.

[58] The excitation of modes in the continuum could result from a number of possible mechanisms. One possibility is that nonlinear effects broaden the wave spectrum near the primary resonance location as seen in the spectrum shown in Figure 8b. The frequency broadened waves could satisfy the resonance condition at a different location. Such waves could leak energy from the primary resonance location to the location where their shifted frequency matches the continuum frequency, leading to a pileup of energy at the shifted resonance location. The nonlinear wave-wave interaction and the conditions for the occurrence of a broad mode conversion region require further investigation beyond the scope of this study.

4. Summary

[59] In this paper, a 2-D hybrid simulation is presented for the interaction between an incident fast mode compressional wave with the magnetopause. Mode conversion from the compressional to KAWs as a results of the interaction is investigated.

[60] As the compressional wave reaches the magnetopause boundary from the magnetosheath, strong KAWs are excited at the location where the Alfvén resonance condition $\omega = k_\parallel V_A(x)(1 - \omega^2/\Omega_i^2)$ is satisfied. These KAWs are short wavelength waves, with $k_\perp\rho_i \sim 1$ and wave number k_x along the magnetopause normal reversing its direction into the magnetosheath. Strong enhancement of B_y, V_{iy}, $J_\parallel$, E_x, and
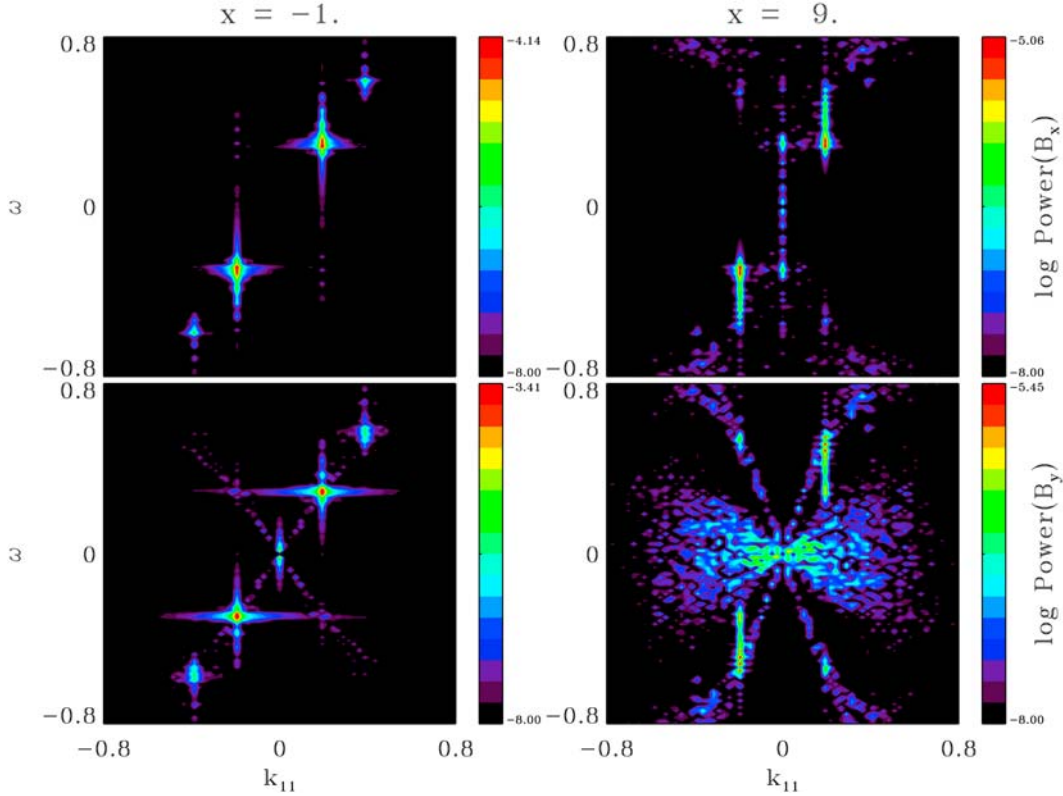
Figure 12. Powers of B_x and B_y in the $k_\parallel$-ω plane at $x = X_r = -1.0$ and $x = 9.0$ obtained in case 5.

parallel electric field $E_\parallel$ are present in the KAWs, in which the density and magnetic field strength are also perturbed. While the KAWs radiate into the magnetosheath, the compressional waves and KAWs undergo a spatial decay on the magnetospheric side of the Alfvén resonance point.

[61] The simulation results are compared with the linear theory of mode conversion, for the location of the mode conversion and the wave properties of the resulting KAWs. The absorption rate of the incident wave because of the mode conversion is estimated as functions of ω_0, θ, D_0, and T_{e0}/T_{i0}. The simulation results are found to agree well with the absorption rate obtained from a theoretical model that solves an analytic solution of the full fluid wave equations in a system containing an equilibrium structure of the magnetopause. According to our study, the absorption rate A increases with θ, but is nonzero even at $\theta = 0°$ as long as $\omega_0 > 10\%$ of the ion cyclotron frequency Ω_s in the magnetosheath. The absorption varies significantly with ω_0, peaking near $\omega_0 \sim 0.3\Omega_s$. The efficiency of the mode conversion process can be greatly enhanced over the MHD limit and for a broad range of frequency, and angle of propagation can capture most of the wave power in the magnetopause boundary layer where it is converted into kinetic Alfvén waves. On the other hand, it has weak dependence on D_0 and T_{e0}/T_{i0}.

[62] In addition to the linear physics, several nonlinear properties of the mode conversion have been obtained from cases with wave amplitude $\delta V_i \sim 0.01$–0.3. The second, third, and higher harmonics of ω_0 are found to be generated in the mode conversion process, in addition to the primary ω_0 of the incident wave. The spatial decay of harmonic modes is faster than that of the primary mode. Moreover, the harmonics can also be generated in the incident wave in the nondispersive manner as the wave steepens before it interacts with the magnetopause.

[63] Nonlinear wave-wave interaction that develops near the primary resonance point can lead to a broadening of the spectrum at the resonance location because the dispersion depends on frequency. In addition, on the high V_A side of the resonance, peaks occur at the local continuum frequency having $k_\parallel = k_{\parallel 0}$ (as well as its harmonics in many cases). Although a broad range of continuum normal modes satisfying $\omega = k_\parallel V_A(x)(1 - \omega^2/\Omega_i^2(x))$ are weakly excited by simulation noise at each location, x, there is a strong peak of the wave spectrum satisfying $\omega = k_{\parallel 0} V_A(1 - \omega^2/\Omega_i^2)$. This continuum mode might be excited by a nonlinear process that broadens the frequency spectrum near the primary resonance (perhaps from wave-particle trapping effects), by parametric excitation of the continuum mode from the large amplitude driver wave, or by some other nonlinear process that has not yet been identified. Regardless of the cause, we have found that nonlinear interactions driven by a monochromatic compressional wave driver lead to a broadened resonant region (basically exciting the entire continuum and not just the primary resonance) in a significantly different manner than the broadening that would result if the incident wave packet had a frequency spectrum with a spectral width. Although, the effects of the broad incident spectral width on the mode conversion are not discussed in this paper, in reality, such effects and the nonlinearity coexist.

[64] Correlated with perturbations in the transverse magnetic field, wavy variations in the ion temperature are also

present in the KAWs. Strong temperature enhancement is found in cases with a relatively large wave amplitude, although the ion heating is not a focus of investigation in this paper. Generation of harmonics could be important for ion heating. Above a threshold wave amplitude, ions can be heated perpendicular to the magnetic field by nonlinear resonance between the polarization drift and gyromotion [*Johnson and Cheng*, 2001; *Chen et al.*, 2001]. The heating efficiency increases with increasing frequency [*White et al.*, 2002]. Heated ions are commonly seen at the magnetopause in conjunction with waves that satisfy the threshold condition for chaotic ion heating [*Chaston et al.*, 2008]. Therefore, the nonlinear excitation of harmonics could increase the efficiency of ion heating and particle transport.

[65] It should be noted that the ion transport due to KAWs cannot be examined with the present hybrid model. The assumption of the quasi-charge neutrality results in $V_{ix} = V_{ex}$, and thus a zero net plasma flux along the magnetopause normal, $\Gamma_x = 0$. By tracing the particle positions in the simulation, the mean square positions of ions relative to the electron fluid elements are found to be virtually zero, although the ions exhibit a displacement in the normal direction as the magnetopause oscillates or shifts position in response to the incident waves. Given that in the hybrid model the electron fluid is frozen in the magnetic field, a null crossfield diffusion of ions would be obtained.

[66] It should also be noted that our model does not include plasma flow in the magnetosheath, so it is more appropriate for the subsolar magnetopause. Plasma flow modifies compressional wave propagation in the sheath and introduces a source of free energy that can also drive Kelvin-Helmholtz instabilities unstable. As a future topic, it would also be interesting to examine the mode conversion process that would occur at the flanks and how the free energy from the plasma flow couples with the Alfvén resonance and the associated plasma transport. It would also be useful to include electron Landau damping in the model, which can be important for particle transport.

References

Anderson, B. J., S. A. Fuselier, S. P. Gary, and R. E. Denton (1994), Magnetic spectral signatures in the Earth's magnetosheath and plasma depletion layer, *J. Geophys. Res.*, *99*, 5877–5891.

Anderson, R. R., C. C. Harvey, M. M. Hoppe, and B. T. Tsurutani (1982), Plasma waves near the magnetopause, *J. Geophys. Res.*, *87*, 2087–2107.

Budden, K. G. (1961), *Radio Waves in the Ionosphere*, Cambridge Univ. Press, Cambridge, U. K.

Chaston, C. C., M. Wilber, F. S. Mozer, M. Fujimoto, M. L. Goldstein, M. Acuna, H. Reme, and A. Fazakerley (2007), Mode conversion and anomalous transport in Kelvin-Helmholtz vortices and kinetic Alfvén waves at the Earth's magnetopause, *Phys. Rev. Lett.*, *99*, 175004.

Chaston, C., et al. (2008), Turbulent heating and cross-field transport near the magnetopause from THEMIS, *Geophys. Res. Lett.*, *35*, L17S08, doi:10.1029/2008GL033601.

Chen, L. (1999), Theory of plasma transport induced by low-frequency hydromagnetic waves, *J. Geophys. Res.*, *104*, 2421–2428.

Chen, L. (2008), Alfvén waves: a journey between space and fusion plasmas, *Plasma Phys. Control. Fusion*, *50*, 124001.

Chen, L., and A. Hasegawa (1974), Plasma heating by spatial resonance of Alfven wave, *Phys. Fluids*, *17*, 1399–1403.

Chen, L., Z. Lin, and R. White (2001), On resonant heating below the cyclotron frequency, *Phys. Plasmas*, *8*, 4713–4716.

Cheng, C. Z., and J. R. Johnson (1999), A kinetic-fluid model, *J. Geophys. Res.*, *104*, 413–428.

Clack, C. T. M., and I. Ballai (2009), Nonlinear resonant absorption of fast magnetoacoustic waves in strongly anisotropic and dispersive plasmas, *Phys. Plasmas*, *16*, 042305.

Clack, C. T. M., I. Ballai, and M. S. Ruderman (2009), On the validity of nonlinear Alfvén resonance in space plasmas, *Astron. Astrophys.*, *494*, 317–327.

Dmitrienko, I. S. (1997), Nonlinear Alfvén resonance, *J. Plasma Phys.*, *57*, 311–326.

Engebretson, M. J., J. L. Cahil Jr., R. L. Arnoldy, B. J. Anderson, T. J. Rosenberg, D. L. Carpenter, U. S. Inan, and R. H. Eather (1991a), The role of the ionosphere in coupling upstream ULF wave power into the dayside magnetosphere, *J. Geophys. Res.*, *96*, 1527–1542.

Engebretson, M. J., N. Lin, W. Baumjohann, H. Luehr, B. J. Anderson, L. J. Zanetti, T. A. Potemra, R. L. McPherron, and M. G. Kivelson (1991b), A comparison of ULF fluctuations in the solar wind, magnetosheath, and dayside magnetosphere: 1. Magnetosheath morphology, *J. Geophys. Res.*, *96*, 3441–3454.

Fairfield, D. H., A. Otto, T. Mukai, S. Kokubun, R. P. Lepping, J. T. Steinberg, A. J. Lazarus, and T. Yamamoto (2000), Geotail observations of the Kelvin-Helmholtz instability at the equatorial magnetotail boundary for parallel northward fields, *J. Geophys. Res.*, *105*, 21,159–21,174.

Fairfield, D. H., C. J. Farrugia, T. Mukai, T. Nagai, and A. Fedorov (2003), Motion of the dusk flank boundary layer caused by solar wind pressure changes and the Kelvin-Helmholtz instability: 10–11 January 1997, *J. Geophys. Res.*, *108*(A12), 1460, doi:10.1029/2003JA010134.

Fairfield, D. H., M. M. Kuznetsova, T. Mukai, T. Nagai, T. I. Gombosi, and A. J. Ridley (2007), Waves on the dusk flank boundary layer during very northward interplanetary magnetic field conditions: Observations and simulation, *J. Geophys. Res.*, *112*, A08206, doi:10.1029/2006JA012052.

Fujimoto, M., T. Terasawa, T. Mukai, Y. Saito, T. Yamamoto, and S. Kokubun (1998), Plasma entry from the flanks of the near-Earth magnetotail, *J. Geophys. Res.*, *103*, 4391–4408.

Fujimoto, M., T. Tonooka, and T. Mukai (2003), Vortex-like fluctuations in the magnetotail flanks and their possible roles in plasma transport, in *Earth's Low-Latitude Boundary Layer*, Geophys. Monogr. Ser., vol. 133, edited by P. Newell and T. Onsager, pp. 241–251, AGU, Washington, D. C.

Hasegawa, A., and L. Chen (1976), Kinetic processes in plasma heating by resonant mode conversion of Alfven wave, *Phys. Fluids*, *19*, 1924–1934.

Hasegawa, A., and K. Mima (1978), Anomalous transport produced by kinetic Alfvén wave turbulence, *J. Geophys. Res.*, *83*, 1117–1123.

Hasegawa, A., K. H. Tsui, and A. S. Assis (1983), A theory of long period magnetic pulsations. III - Local field line oscillations, *Geophys. Res. Lett.*, *10*, 765–767.

Hasegawa, H., K. Maezawa, T. Mukai, and Y. Saito (2002a), Plasma entry across the distant tail magnetopause: 2. Comparison between MHD theory and observation, *J. Geophys. Res.*, *107*(A6), 1073, doi:10.1029/2001JA900138.

Hasegawa, H., K. Maezawa, T. Mukai, and Y. Saito (2002b), Plasma entry across the distant tail magnetopause: 1. Global properties and IMF dependence, *J. Geophys. Res.*, *107*(A5), 1063, doi:10.1029/2001JA900139.

Hasegawa, H., M. Fujimoto, K. Maezawa, Y. Saito, and T. Mukai (2003), Geotail observations of the dayside outer boundary region, *J. Geophys. Res.*, *108*(A4), 1163, doi:10.1029/2002JA009667.

Hasegawa, H., M. Fujimoto, T.-D. Phan, H. Rème, A. Balogh, M. W. Dunlop, C. Hashimoto, and R. TanDokoro (2004), Transport of solar wind into Earth's magnetosphere through rolled-up Kelvin-Helmholtz vortices, *Nature*, *430*, 755–758.

Hasegawa, H., M. Fujimoto, K. Takagi, Y. Saito, T. Mukai, and H. Rème (2006), Single-spacecraft detection of rolled-up Kelvin-Helmholtz vortices at the flank magnetopause, *J. Geophys. Res.*, *111*, A09203, doi:10.1029/2006JA011728.

Johnson, J. R. (1992), Excitation of low frequency turbulence along auroral field lines, Ph.D. thesis, Mass. Inst. of Technol., Cambridge.

Johnson, J. R., and C. Z. Cheng (1997), Kinetic Alfvén waves and plasma transport at the magnetopause, *Geophys. Res. Lett.*, *24*, 1423–1426.

Johnson, J. R., and C. Z. Cheng (2001), Stochastic ion heating at the magnetopause due to kinetic Alfvén waves, *Geophys. Res. Lett.*, *28*, 4421–4424.

Johnson, J. R., and S. Wing (2009), Northward IMF Plasma sheet entropies, *J. Geophys. Res.*, *114*, A00D08, doi:10.1029/2008JA014017.

Johnson, J. R., C. Z. Cheng, and P. Song (2001), Signatures of mode conversion and kinetic Alfvén waves at the magnetopause, *Geophys. Res. Lett.*, *28*, 227–230.

Karney, C. F. F., F. W. Perkins, and Y.-C. Sun (1979), Alfven resonance effects on magnetosonic modes in large tokamaks, *Phys. Rev. Lett.*, *42*, 1621–1624.

Labelle, J., and R. A. Treumann (1988), Plasma waves at the dayside magnetopause, *Space. Sci. Rev.*, *47*, 175–202.

Lavraud, B., M. F. Thomsen, S. Wing, M. Fujimoto, M. H. Denton, J. E. Borovsky, A. Aasnes, K. Seki, and J. M. Weygand (2006), Observation of two distinct cold, dense ion populations at geosynchronous orbit: Local time asymmetry, solar wind dependence and origin, *Ann. Geophys.*, *24*, 3451–3465.

Le, G., C. T. Russell, J. T. Gosling, and M. F. Thompsen (1996), ISEE observations of low-latitude boundary layer for northward interplanetary magnetic field: Implications for cusp reconnection, *J. Geophys. Res.*, *101*, 27,239–27,249.

Lee, L. C., J. R. Johnson, and Z. W. Ma (1994), Kinetic Alfvén waves as a source of plasma transport at the dayside magnetopause, *J. Geophys. Res.*, *99*, 17,405–17,411.

Lin, N., M. J. Engebretson, R. L. McPherron, M. G. Kivelson, W. Baumjohann, H. Luehr, T. A. Potemra, B. J. Anderson, and L. J. Zanetti (1991), A comparison of ULF fluctuations in the solar wind, magnetosheath, and dayside magnetosphere. II. Field and plasma conditions in the magnetosheath, *J. Geophys. Res.*, *96*, 3455–3464.

Lin, Y., and X. Y. Wang (2005), Three-dimensional global hybrid simulation of dayside dynamics associated with the quasi-parallel bow shock, *J. Geophys. Res.*, *110*, A12216, doi:10.1029/2005JA011243.

Lin, Y., and H. Xie (1997), Formation of reconnection layer at the dayside magnetopause, *Geophys. Res. Lett.*, *24*, 3145–3148.

Majeski, R., C. K. Phillips, and J. R. Wilson (1994), Electron heating and current drive by mode converted slow waves, *Phys. Rev. Lett.*, *73*, 2204–2207.

Nakamura, T. T., and M. Fujimoto (2002), Electron inertia effects in an MHD scale Kelvin-Helmholtz vortex, *Eos Trans. AGU*, *83*(47), Fall Meet. Suppl., Abstract SM11B-0435.

Nykyri, K., and A. Otto (2001), Plasma transport at the magnetospheric boundary due to reconnection in Kelvin-Helmholtz vortices, *Geophys. Res. Lett.*, *28*, 3565–3568.

Nykyri, K., A. Otto, B. Lavraud, C. Mouikis, L. M. Kistler, A. Balogh, and H. Rème (2006), Cluster observations of reconnection due to the Kelvin-Helmholtz instability at the dawnside magnetospheric flank, *Ann. Geophys.*, *24*, 2619–2643.

Ogilvie, K. W., and R. J. Fitzenreiter (1989), The Kelvin-Helmholtz instability at the magnetopause and inner boundary layer surface, *J. Geophys. Res.*, *94*, 15,113–15,123.

Øieroset, M., T. Phan, M. Fujimoto, L. Chan, R. P. Lin, and R. Skoug (2003), Spatial and temporal variations in the cold dense plasma sheet: Evidence for a low-latitude boundary layer source, in *Earth's Low-Latitude Boundary Layer*, *Geophys. Monogr. Ser.*, vol. 133, edited by P. Newell and T. Onsager, pp. 253–264AGU, Washington, D. C.

Øieroset, M., J. Raeder, T. D. Phan, S. Wing, J. P. McFadden, W. Li, M. Fujimoto, H. Rème, and A. Balogh (2005), Global cooling and densification of the plasma sheet during an extended period of purely northward IMF on October 22–24, 2003, *Geophys. Res. Lett.*, *32*, L12S07, doi:10.1029/2004GL021523.

Otto, A., and D. H. Fairfield (2000), Kelvin-Helmholtz instability at the magnetotail boundary: MHD simulation and comparison with Geotail observations, *J. Geophys. Res.*, *105*, 21,175–21,190.

Phan, T.-D., G. Paschmann, W. Baumjohann, N. Sckopke, and H. Luehr (1994), The magnetosheath region adjacent to the dayside magnetopause: AMPTE/IRM observations, *J. Geophys. Res.*, *99*, 121–141.

Phan, T.-D., G. Paschmann, and B. U. Ö. Sonnerup (1996a), Low-latitude dayside magnetopause and boundary layer for high magnetic shear: 2. Occurrence of magnetic reconnection, *J. Geophys. Res.*, *101*, 7817–7828.

Phan, T. D., et al. (1996b), The subsolar magnetosheath and magnetopause for high solar wind ram pressure: WIND observations, *Geophys. Res. Lett.*, *23*, 1279–1282.

Phan, T. D., R. P. Lin, S. A. Fuselier, and M. Fujimoto (2000), Wind observations of mixed magnetosheath-plasma sheet ions deep inside the magnetosphere, *J. Geophys. Res.*, *105*, 5497–5506.

Raeder, J., J. Berchem, M. Ashour-Abdalla, L. A. Frank, W. R. Paterson, K. L. Ackerson, S. Kokubun, T. Yamamoto, and J. A. Slavin (1997), Boundary layer formation in the magnetotail, *Geophys. Res. Lett.*, *24*, 951–954.

Ram, A. K., and A. Bers (1996), Current drive by mode-converted Ion-Bernstein waves, *APS Meet. Abstr.*

Rezeau, L., S. Perraut, and A. Roux (1986), Electromagnetic fluctuations in the vicinity of the magnetopause, *Geophys. Res. Lett.*, *13*, 1093–1096.

Rezeau, L., A. Morane, S. Perraut, A. Roux, and R. Schmidt (1989), Characterization of Alfvenic fluctuations in the magnetopause boundary layer, *J. Geophys. Res.*, *94*, 101–110.

Rezeau, L., A. Roux, and C. T. Russell (1993), Characterization of small-scale structures at the magnetopause from ISEE measurements, *J. Geophys. Res.*, *98*, 179–186.

Song, P. (1994), ISEE observations of the dayside magnetosheath, *Adv. Space Res.*, *14*, 71–80.

Song, P., and C. T. Russell (1992), A model for the formation of the low-latitude boundary layer, *J. Geophys. Res.*, *97*, 1411–1420.

Song, P., C. T. Russell, and C. Y. Huang (1993a), Wave properties near the subsolar magnetopause - Pc 1 waves in the sheath transition layer, *J. Geophys. Res.*, *98*, 5907–5923.

Song, P., C. T. Russell, R. J. Strangeway, J. R. Wygant, C. A. Cattell, R. J. Fitzenreiter, and R. R. Anderson (1993b), Wave properties near the subsolar magnetopause: Pc 3–4 energy coupling for northward interplanetary magnetic field, *J. Geophys. Res.*, *98*, 187–196.

Song, P., et al. (1993c), Structure and properties of the subsolar magnetopause for northward interplanetary magnetic field: Multiple-instrument particle observations, *J. Geophys. Res.*, *98*, 11,319–11,337.

Song, P., C. T. Russell, and S. P. Gary (1994), Identification of low-frequency fluctuations in the terrestrial magnetosheath, *J. Geophys. Res.*, *99*, 6011–6025.

Southwood, D. J. (1974), Some features of field line resonances in the magnetosphere, *Planet. Space Sci.*, *22*, 483–491.

Stix, T. H. (1992), *Waves in Plasmas*, Am. Inst. of Phys., New York.

Streltsov, A. V., W. Lotko, J. R. Johnson, and C. Z. Cheng (1998), Small-scale, dispersive field line resonances in the hot magnetospheric plasma, *J. Geophys. Res.*, *103*, 26,559–26,572.

Swanson, D. G. (1989), *Plasma Waves*, Academic, San Diego, Calif.

Swift, D. W. (1996), Use of a hybrid code for a global-scale plasma simulation, *J. Comput. Phys.*, *126*, 109–121.

Takahashi, K., D. G. Sibeck, P. T. Newell, and H. E. Spence (1991), ULF waves in the low-latitude boundary layer and their relationship to magnetospheric pulsations: A multisatellite observation, *J. Geophys. Res.*, *96*, 9503–9519.

Tamao, T. (1965), Transmission and coupling resonance of hydromagnetic disturbances in the non-uniform Earth's magnetosphere, *Sci. Rep. Tohoku Univ., Ser. 5, Geophys.*, *17*, 43.

Thomas, V. A., and D. Winske (1991), Kinetic simulation of the Kelvin-Helmholtz instability at the Venus ionopause, *Geophys. Res. Lett.*, *18*, 1943–1946.

Thomas, V. A., and D. Winske (1993), Kinetic simulations of the Kelvin-Helmholtz instability at the magnetopause, *J. Geophys. Res.*, *98*, 11,425–11,438.

Tsurutani, B. T., and R. M. Thorne (1982), Diffusion processes in the magnetopause boundary layer, *Geophys. Res. Lett.*, *9*, 1247–1250.

Uberoi, C. (1972), Alfvén waves in inhomogeneous magnetic fields, *Phys. Fluids*, *15*, 1673–1675.

Wang, C.-P., L. R. Lyons, T. Nagai, J. M. Weygand, and R. W. McEntire (2007), Sources, transport, and distributions of plasma sheet ions and electrons and dependences on interplanetary parameters under northward interplanetary magnetic field, *J. Geophys. Res.*, *112*, A10224, doi:10.1029/2007JA012522.

White, R., L. Chen, and Z. Lin (2002), Resonant plasma heating below the cyclotron frequency, *Phys. Plasmas*, *9*, 1890–1897.

Wing, S., and P. T. Newell (2002), 2D plasma sheet ion density and temperature profiles for northward and southward IMF, *Geophys. Res. Lett.*, *29*(9), 1307, doi:10.1029/2001GL013950.

Wing, S., and P. T. Newell (2003), LLBL contribution to the plasma sheet ions, in *Earth's Low-Latitude Boundary Layer*, *Geophys. Monogr. Ser.*, vol. 133, edited by P. Newell and T. Onsager, pp. 273–282, AGU, Washington, D. C.

Wing, S., J. R. Johnson, P. T. Newell, and C.-I. Meng (2005), Dawn-dusk asymmetries, ion spectra, and sources in the northward interplanetary magnetic field plasma sheet, *J. Geophys. Res.*, *110*, A08205, doi:10.1029/2005JA011086.

Winglee, R. M. (1982), Finite frequency effects on magnetosonic wave mode conversion, *Plasma Phys.*, *24*, 1161–1168.

J. R. Johnson, Princeton Plasma Physics Laboratory, Princeton University, Princeton, NJ 08543, USA. (jrj@pppl.gov)

Y. Lin and X. Y. Wang, Physics Department, Auburn University, 206 Allison Laboratory, Auburn, AL 36849-5311, USA. (ylin@physics.auburn.edu; xywang@physics.auburn.edu)